

# Effects of Saharan Dust on the Linear Dynamics of African Easterly Waves

DUSTIN F. P. GROGAN, TERRENCE R. NATHAN, AND SHU-HUA CHEN

*Atmospheric Science Program, Department of Land, Air, and Water Resources, University of California, Davis,  
Davis, California*

(Manuscript received 27 May 2015, in final form 13 November 2015)

## ABSTRACT

The direct radiative effects of Saharan mineral dust aerosols on the linear dynamics of African easterly waves (AEWs) are examined analytically and numerically. The analytical analysis combines the thermodynamic equation with a dust continuity equation to form an expression for the dust-modified generation of eddy available potential energy  $\overline{GE}$ . The dust-modified  $\overline{GE}$  is a function of the transmissivity and spatial gradients of the dust, which are modulated by the Doppler-shifted frequency. The expression for  $\overline{GE}$  predicts that for a fixed dust distribution, the wave response will be largest in regions where the dust gradients are maximized and the Doppler-shifted frequency vanishes. The numerical analysis uses the Weather Research and Forecasting (WRF) Model coupled to an online dust model to calculate the linear dynamics of AEWs. Zonally averaged basic states for wind, temperature, and dust are chosen consistent with summertime conditions over North Africa. For the fastest-growing AEW, the dust increases the growth rate from  $\sim 15\%$  to  $90\%$  for aerosol optical depths ranging from  $\tau = 1.0$  to  $\tau = 2.5$ . A local energetics analysis shows that for  $\tau = 1.0$ , the dust increases the maximum barotropic and baroclinic energy conversions by  $\sim 50\%$  and  $\sim 100\%$ , respectively. The maxima in the generation and conversions of energy are collocated and occur where the meridional dust gradient is maximized near the critical surface—that is, where the Doppler-shifted frequency is small, in agreement with the prediction from the analytical analysis.

## 1. Introduction

The summertime circulation over North Africa is a complex system composed of many features, including monsoonal flows, dust storms, and easterly jets. The system regularly produces westward-propagating, synoptic-scale waves—termed African easterly waves (AEWs)—that mostly grow from the barotropic–baroclinic instability of the African easterly jet (AEJ; Burpee 1972; Hsieh and Cook 2005). The AEWs that develop on the AEJ are characterized by pronounced signatures at midlevels ( $\sim 600$  hPa) south of the AEJ and at low levels ( $\sim 850$  hPa) north of the AEJ (Carlson 1969; Pytharoulis and Thorncroft 1999). As the AEWs move westward toward the Atlantic Ocean, their north and south signatures often merge to form a single structure (Ross and Krishnamurti 2007; Hankes et al. 2015). The single structured AEWs have been shown to

be involved in more than half of the tropical cyclones that developed over the eastern Atlantic Ocean (Frank 1970; Landsea 1993; Chen and Liu 2014).

The AEWs also contribute to the episodic formation of synoptic-scale plumes of Saharan mineral dust aerosols (Jones et al. 2003; Knippertz and Todd 2010). The plumes propagate from their Saharan origin to affect regions as far away as the Caribbean and North America (Prospero and Carlson 1972; Prospero 1999). Throughout their lifetime, the plumes modify the radiative and microphysical properties<sup>1</sup> of the atmosphere to affect the energy budget (Zhu et al. 2007). The dust-modified energy budgets, in turn, can affect the synoptic-scale circulation over North Africa (Tompkins et al. 2005; Wilcox et al. 2010; Reale et al. 2011) and the eastern Atlantic Ocean (Karyampudi and Pierce 2002; Chen et al. 2010; Bretl et al. 2015).

For example, Chen et al. (2010) used the Weather Research and Forecasting (WRF) Model coupled to an online dust model to show that direct dust–radiative

---

*Corresponding author address:* Dustin Grogan, Atmospheric Science Program, Department of Land, Air, and Water Resources, One Shields Avenue, University of California, Davis, CA 95616-8627.

E-mail: [dfgrogan@ucdavis.edu](mailto:dfgrogan@ucdavis.edu)

DOI: 10.1175/JAS-D-15-0143.1

---

<sup>1</sup> The effects of dust on the energy budget are often distinguished by direct radiative effects and indirect microphysical effects. Here we examine the former.

forcing can affect the environmental shear over the eastern Atlantic Ocean. In this region the cool, moist marine layer undercuts the hot, dry air that originated over the Sahara Desert. This elevated layer—known as the Saharan air layer (SAL)—contains Saharan mineral dust that varies in space and time. The dust concentrations, measured by aerosol optical depth (AOD), can be as low as  $\sim 0.2$  and reach values as large as  $\sim 4.0$  (Koch et al. 2012). Chen et al. (2010) found that the dust modifies the temperature field within the SAL, which, through thermal wind balance, changes the environmental wind shear. They showed that south of the dust-modified SAL, where AEWs are often found, there was an expansion of the layer of maximum vertical wind shear: the vertical shear of the zonal wind increased by about  $1\text{--}2.5\text{ m s}^{-1}\text{ km}^{-1}$  between  $\sim 650$  and  $500\text{ hPa}$ , causing a  $\sim 3\text{--}5\text{ m s}^{-1}$  (30%–40%) increase in the maximum wind speed.

The direct radiative effects of Saharan dust on AEWs are less clear. For example, some studies suggest that dust weakens the growth of AEWs (Karyampudi and Carlson 1988; Reale et al. 2009; Jury and Santiago 2010; Ismail et al. 2010); other studies suggest that dust strengthens the growth of AEWs (Jones et al. 2004; Lavaysse et al. 2011; Ma et al. 2012). A study even finds that the dust may strengthen or weaken the growth of the AEWs depending on the position of the AEWs relative to the dust field (Hosseinpour and Wilcox 2014).

Consider first the studies that show dust weakens AEWs. Karyampudi and Carlson (1988) used a regional tropical model to examine the propagation and growth of AEWs along the southern boundary of the SAL. They found that a dust-laden SAL weakens the transverse/vertical circulations that contribute to the growth of AEWs. The modeling study by Reale et al. (2009) and the statistical study by Jury and Santiago (2010) also found that dust-laden SALs weaken the growth of AEWs, but their studies focused on a different mechanism, one that hinges on the SAL being drawn into the AEW environment. Specifically, an increase in the dust concentration within the SAL increases the dust–radiative heating rate, leading to an increase in temperature. As the dust-warmed SAL is drawn into the AEW environment, the midlevel increase in temperature relative to that below increases the static stability. The result is a more stable environment, one that weakens the growth of AEWs.

In sharp contrast to the studies cited above that show dust weakens AEWs, Jones et al. (2004) found that a dust-modified environment may strengthen the growth of AEWs. Using 22 years of NCEP–NCAR reanalysis

and dust from a global transport model, Jones et al. (2004) provided indirect observational evidence that the enhanced growth of AEWs over the Atlantic Ocean results from a reduction in static stability caused by dust-induced warming in the lower troposphere. Ma et al. (2012) used the WRF Model with prescribed dust profiles and, like Jones et al. (2004), found that the dust–radiative forcing reduces the static stability, which they suggest is due to the trapping and reabsorption of longwave radiation near the bottom of the dust layer. Ma et al. (2012) concluded that this dust–radiative warming enhances the convective available potential energy for shallow convection in the AEW environment, which “serves as a catalyst to promote local convection that facilitates AEW development.” The dust-induced development, however, occurred for most but not all of the waves studied by Ma et al. (2012).

Despite the differences in the above studies, they share an underlying commonality: none have examined the interactions between the wave fields in dust, wind, and temperature, interactions that we will show are important to the growth and structure of AEWs. That such radiative–dynamical interactions are important to AEWs may not be surprising, since previous studies have shown that shortwave absorbers can directly affect the linear characteristics of a wide variety of free and forced waves. These waves range from equatorial gravity waves (Zhu and Holton 1986; Cordero et al. 1998; Grogan et al. 2012) to midlatitude planetary waves (Ghan 1989a,b; Nathan 1989; Nathan and Li 1991; Nathan and Cordero 2007). These studies all show that the tracer-modified wave characteristics are due to the radiative heating produced by the tracer, which depends on feedbacks involving the advection of the background absorber by the wave field as well as the sources and sinks of the absorber. Although these feedbacks also operate in the interactions between Saharan dust and AEWs, several unanswered questions are unique to the dust–AEW problem. For example, is there a location of the basic state dust field relative to the AEJ that optimizes the growth of AEWs? What is the relative importance of meridional versus vertical advection of dust in modifying the linear characteristics of AEWs? And what role do critical surfaces play in the dust-modified linear dynamics of AEWs?

To answer these questions, we use the Weather Research and Forecasting Model coupled to an online dust model to determine the direct radiative effects of Saharan mineral dust aerosols on the linear stability characteristics of AEWs. Our stability analysis focuses on North Africa, where the

synoptic-scale plumes of Saharan dust and AEWs both originate.

The paper is organized as follows: [Section 2](#) describes the model, basic states, and methods for the numerical experiments. In [section 3](#) an expression is derived for the generation of eddy available potential energy that exposes the physics of the dust–radiative interactions. The expression is used to interpret the numerical results presented in [section 4](#). Finally, [section 5](#) summarizes the main conclusions.

## 2. Model and basic states

### a. Model

Our numerical experiments are based on the WRF dust model developed by [Chen et al. \(2015\)](#). The model consists of the WRF dynamical core coupled to an online dust model. The dust model consists of 12 continuity equations for dust particle radii spanning 0.15–5  $\mu\text{m}$ . The governing equations are written in flux form on terrain-following coordinates to conserve mass and energy. Dust radiative fluxes are calculated using the NASA Goddard Space Flight Center (GSFC) radiation model, which inputs dust optical properties—*aerosol optical depth, single scattering albedo, and asymmetry parameter*—that are calculated using the *Optical Properties of Aerosol and Clouds (OPAC)* software packages ([Hess et al. 1998](#)). The GSFC model computes daily averaged dust–radiative diabatic heating–rate profiles, which accounts for the effects of shortwave heating due to dust absorption and scattering, longwave cooling due to dust, and the reabsorption of the longwave radiation by other constituents.

To examine the dust-modified linear dynamics of AEWs, we have modified the [Chen et al. \(2015\)](#) WRF dust model in the following ways: 1) The model experiments are hydrostatic and linear (the linearization process is described in [section 4a](#)). 2) Each of the 12 dust continuity equations depend only on the advection and sedimentation of dust; several parameterized effects of dust are excluded—that is, subgrid cumulus and boundary layer mixing, surface emission, and wet and dry deposition. 3) Following [Carlson and Benjamin \(1980\)](#), the dust-heating-rate profile is computed by subtracting the daily averaged reference, dust-free heating rate due to atmospheric constituents (*i.e.*, moisture, ozone,  $\text{CO}_2$ , etc.) from the total heating rate due to dust and the other atmospheric constituents. The GSFC model provides the reference profiles for the constituents, except moisture. We impose the moisture profile, as described in [section 2b](#) below.

The model domain is a global channel projected onto a cylindrical-equidistant grid that extends from 10°S to 40°N. The horizontal resolution is 0.5° and the time step is 3 min in order to satisfy the Courant–Friedrichs–Lewy (CFL) criteria. In the vertical the model is divided into 50 terrain-following levels with the pressure equal to 100 hPa at the model top; there is no topography. The boundary conditions are periodic in the east–west direction, symmetric at the north and south channel walls, and free slip at the top and bottom boundaries. A 30-min hyper diffusion is imposed on the wind fields.

### b. Basic states

The basic state zonal wind and temperature fields are representative of summertime conditions over North Africa. The basic state dust field is representative of well-mixed plumes observed in the lower atmosphere over the Sahara Desert. The zonally averaged basic states for wind, potential temperature and dust are constructed from the analytical functions shown in [appendix A](#).

To ensure the basic states are balanced in the model, we follow [Hall et al.’s \(2006\)](#) approach and introduce, in the wave-free system, a forcing for each of the prognostic fields. The basic state equations can be written as

$$\frac{d\mathbf{X}}{dt} = \mathbf{F}_0 + \mathbf{F}_B, \quad (2.1)$$

where  $\mathbf{X}$  is a state vector that contains the wind, temperature, and dust fields,  $\mathbf{F}_0$  contains all the original forcings for  $\mathbf{X}$ , and  $\mathbf{F}_B$  is the forcing that ensures each field is balanced.

[Figure 1](#) shows the basic state wind and potential temperature fields. The strength and structure of these fields are the primary determinant of the growth and propagation of AEWs ([Burpee 1972](#); [Thorncroft and Hoskins 1994](#)). We have chosen these basic state fields to be consistent with previous studies (see [Table 1](#)). Specifically, the AEJ is symmetric in latitude and asymmetric in height; the jet core is centered at 650 hPa and 15°N latitude and has a maximum speed of 15  $\text{m s}^{-1}$ . The basic state potential temperature field is constructed to satisfy thermal wind balance (see [appendix A](#)), in which case  $\mathbf{F}_B$  is zero in (2.1).

The same basic state wind is used for all of the numerical experiments, irrespective of the basic state dust–radiative forcing. This ensures that any dust-induced changes to the waves are due to the feedbacks involving the wave fields in wind, temperature,

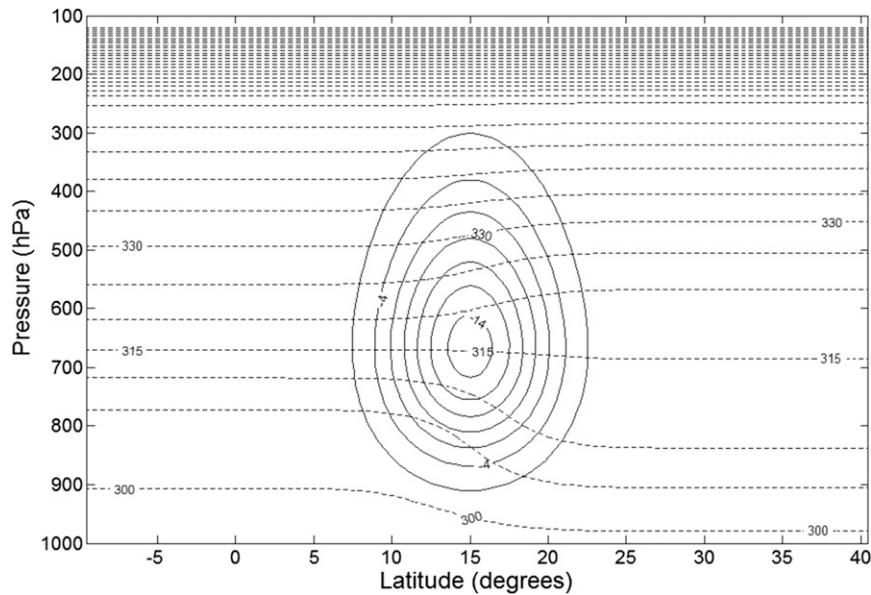


FIG. 1. Basic state distributions of zonal-mean wind (solid) and zonal-mean potential temperature (dashed). Contour intervals are  $2 \text{ m s}^{-1}$  for the wind and  $5 \text{ K}$  for the temperature.

and dust and not to changes in the basic state. As discussed in [Cho and Jenkins \(1987\)](#), the fixed basic state approach is valid if the ratio of diabatic-induced divergences to the relative vorticity is weak. This is the case here; the ratio is  $O(10^{-2})$  for our representative dust field.

The basic state dust distribution for each of the 12 particle sizes is shown in [Fig. 2](#), which is consistent with observations ([Moulin and Chiapello 2004](#); [Kaufman et al. 2005](#)) and previous modeling studies ([Carlson and Benjamin 1980](#); [Konare et al. 2008](#); [Ma et al. 2012](#)). Three features characterize the dust distribution: latitude–height structure, dust concentration, and particle size distribution. In the vertical, the mixing ratio is constant throughout the boundary layer and decreases above. The maximum dust concentration for each dust particle size is  $18 \mu\text{g kg}^{-1}$ , which produces a total maximum dust concentration of  $216 \mu\text{g kg}^{-1}$ . This total value, which is close to the maximum concentration modeled in the zonal-mean summer climatology for dust shown in [Konare et al. \(2008\)](#), yields a shortwave ( $0.5 \mu\text{m}$ ) AOD of  $\sim 1.0$ . An AOD of 1.0 is a conservative value compared to the observed AODs associated with very strong dust emissions over the Sahara Desert, which can reach values as large as 4.0 ([Kochua et al. 2012](#)). Because the primary latitude belt for dust emission is  $\sim 18^\circ\text{--}22^\circ\text{N}$  ([Engelstaedter and Washington 2007](#)), the model plume is centered at  $20^\circ\text{N}$  and chosen to have a symmetric Gaussian distribution in the meridional direction with a half-width of  $\sim 2.5^\circ$ .

The basic state daily averaged dust heating rate, which is computed using the basic state dust field shown in [Fig. 2](#), is shown as solid contours in [Fig. 3](#). Also shown in [Fig. 3](#) is the reference water vapor profile (dotted) used to compute the dust heating rate, which distinguishes the dry Sahara from the moist Sahel; the analytical function for the water vapor profile is given in [appendix A](#). For computational efficiency, the dust heating rate shown in [Fig. 3](#) is computed using a declination angle of  $15^\circ$  and a solar zenith angle of  $30.5^\circ$ , which best represents the daily averaged summer profile that we have computed using 144 evenly spaced solar zenith angles. For these values, the dust heating-rate profile at  $20^\circ\text{N}$  in [Fig. 3](#) closely resembles the desert case from [Carlson and Benjamin \(1980\)](#). Our heating-rate profile differs from [Carlson and Benjamin \(1980\)](#) by only  $0.2 \text{ K day}^{-1}$  near the top of the plume while both heating-rate profiles decrease to  $0.5 \text{ K day}^{-1}$  at the surface.

### 3. Analytical framework

To ease interpretation of the numerical results presented in [section 4](#), we derive an analytical expression for the generation of eddy available potential energy by direct dust–radiative feedbacks  $\text{GE}$ . The expression shows how the spatial distribution of dust and the Doppler-shifted frequency combine to affect the energetics of AEWs.

Consider a flow linearized about a steady, zonally averaged wind that is in radiative equilibrium. The

TABLE 1. Features of the modeled zonal-mean AEJ from select studies that have also considered the linear stability characteristics of AEWs. The shear values correspond to south and north of the jet and below and above the jet. Note: characteristics are listed for the B2 profile in Kwon (1989) and the Greenwich section (GWS) profile in Hall et al. (2006).

Reference	AEJ characteristics			
	Latitude (°)	Pressure level (hPa)	Intensity (m s <sup>-1</sup> )	Shear (south/north) × 10 <sup>-5</sup> s <sup>-1</sup> ; (below/above) × 10 <sup>-3</sup> s <sup>-1</sup>
Rennick (1976)	14	600	14	(4.2/1.2) (11.2/1.0)
Kwon (1989)	20	620	17.7	(2.3/0.9) (6.0/1.8)
Thorncroft and Hoskins (1994)	15	600	15	(2.1/1.7) (4.6/4.1)
Paradis et al. (1995)	15	680	15	(2.5/2.5) (6.0/2.5)
Hall et al. (2006)	12	600	11	(0.7/0.9) (3.5/1.0)
Current study	15	650	15	(2.1/2.1) (5.0/2.0)
Range	12–20	680–600	11–17.7	(0.7–4.2/0.9–2.5) (3.5–11.2/1.0–4.1)

corresponding coupled perturbation equations for temperature and dust mass mixing ratio in isobaric coordinates are

$$\left(\frac{\partial}{\partial t} + \bar{u} \frac{\partial}{\partial x}\right) T + v \frac{\partial \bar{T}}{\partial y} - \omega \bar{S} = \frac{\dot{q}}{c_p} \quad \text{and} \quad (3.1)$$

$$\left(\frac{\partial}{\partial t} + \bar{u} \frac{\partial}{\partial x}\right) \gamma + v \frac{\partial \bar{\gamma}}{\partial y} + \omega \frac{\partial \bar{\gamma}}{\partial p} = \dot{d}. \quad (3.2)$$

The overbar denotes a zonal average;  $\mathbf{x} = (x, y)$ , where  $x$  and  $y$  are the zonal and meridional directions and  $p$  is pressure;  $u(\mathbf{x}, p, t)$ ,  $v(\mathbf{x}, p, t)$  represent the zonal and meridional velocities, and  $\omega(\mathbf{x}, p, t) = dp/dt$  is the vertical motion;  $T(\mathbf{x}, p, t)$  is the temperature;  $\gamma(\mathbf{x}, p, t)$  is the dust mass mixing ratio; and  $\bar{S}(y, p) = -\bar{T}\bar{\theta}^{-1}\partial\bar{\theta}/\partial p$  is the static stability, where  $\bar{\theta}(y, p)$  is the basic state potential temperature.

In (3.1) the dust heating rate per unit mass is given by  $\dot{q}(\mathbf{x}, p, t)$ . For our numerical experiments, the dust heating rate incorporates both shortwave and longwave radiative processes, as described in section 2a. To derive an analytical expression for  $\overline{GE}$ , we only include the shortwave heating. This is a reasonable assumption since Carlson and Benjamin (1980) have shown that over the Sahara Desert, the daily averaged shortwave heating by dust is about an order of magnitude larger than the longwave effects, a result that we have independently confirmed in our model experiments. Recall from section 2a that the shortwave heating is due to absorption and scattering by dust. For simplicity, we neglect scattering for our analytical analysis. As shown by Nathan and Li (1991) and Ghan (1989b), for a trace absorber the perturbation shortwave heating rate, which includes local and nonlocal effects, can be written as

$$\dot{q}(\mathbf{x}, p, t) = A\gamma, \quad (3.3)$$

where  $A(y, p; \bar{\gamma})$ , termed the transmissivity coefficient, is positive<sup>2</sup> and a function of the solar zenith angle, vertical scale of the wave, transmissivity, and aerosol optical depth of the zonal-mean dust distribution [see, for example, (2.6)–(2.7) in Ghan (1989b)]. The detailed representation of  $A(y, p; \bar{\gamma})$  is not important for the qualitative interpretation of the dust-modified generation of eddy available potential energy presented below.

In (3.2) the eddy dust mixing ratio depends on the advection of the eddy dust by the mean flow, the advection of the mean dust by the eddy wind fields, and the dust sources and sinks. The rate of generation or depletion of the eddy dust field is given by  $\dot{d}(\mathbf{x}, p, t)$ . To mimic the dust sedimentation in the numerical model, for our analytical analysis we use a linear damping rate for the perturbation dust, which can be represented as

$$\dot{d}(\mathbf{x}, p, t) = D\gamma, \quad (3.4)$$

where  $D$  is a positive constant.

Appendix B shows the steps taken to derive  $\overline{GE}$  from (3.1)–(3.4). Briefly, these steps involve combining (3.1)–(3.4) into one equation, assuming normal mode solutions for the perturbations to obtain an expression of the eddy dust heating rate, multiplying the eddy heating rate by the eddy temperature field and then zonally averaging. This yields an expression for  $\overline{GE}$  that depends on the phasing between the meridional wind and temperature. In the region below the jet, where the dust is located, the wind and temperature are out of phase, which yields the following expression for  $\overline{GE}$ :

<sup>2</sup>The transmissivity coefficient  $A(y, p; \bar{\gamma})$  may be negative if the dust optical depth is sufficiently large (Ghan 1989b). This is not the case in this study.

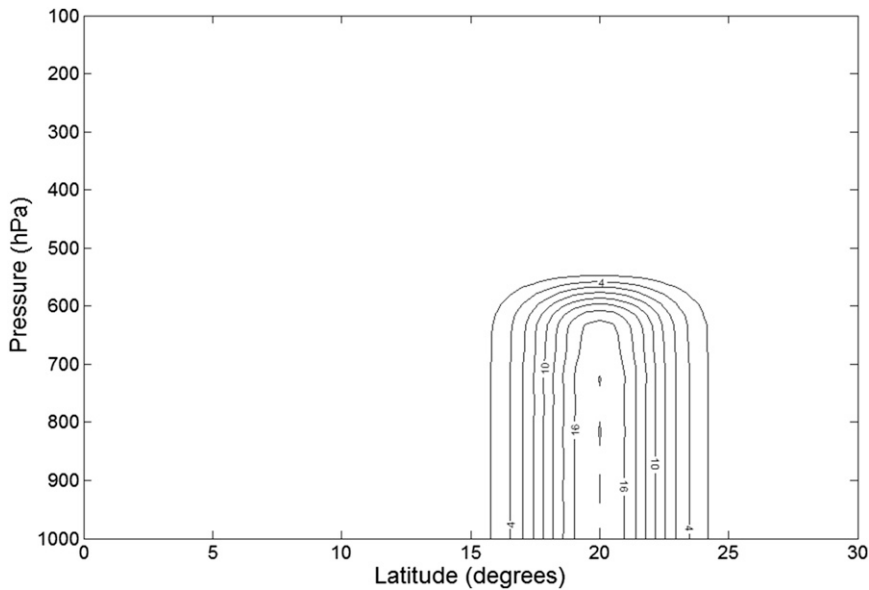


FIG. 2. Basic state dust mass mixing ratio, which is the same for all 12 dust particle sizes (see section 2a). The contour interval is  $2.0 \mu\text{g kg}^{-1}$ . Maximum dust concentration is  $18.0 \mu\text{g kg}^{-1}$ , which is located between 1000 and 700 hPa along  $20^\circ\text{N}$ .

$$\overline{\text{GE}} = G_1|v||T| + G_2|T|^2, \tag{3.5}$$

$$G_1 = C\sigma_i \left( \alpha_y + \frac{pf}{R} \frac{\partial \bar{u}}{\partial p} \alpha_p \right), \text{ and} \tag{3.6a}$$

$$G_2 = -C(\sigma_i kc_i + \sigma_r^2) \alpha_p, \tag{3.6b}$$

where

$$C = \frac{1}{2c_p \bar{S}(\sigma_r^2 + \sigma_i^2)} \exp(2kc_i t), \tag{3.7}$$

$$\alpha_y(y, p; \bar{\gamma}) = A \frac{\partial \bar{\gamma}}{\partial y}, \tag{3.8a}$$

$$\alpha_p(y, p; \bar{\gamma}) = \frac{A}{\bar{S}} \frac{\partial \bar{\gamma}}{\partial p}, \tag{3.8b}$$

$$\sigma_i = \left( kc_i - \frac{\alpha_p}{c_p} + D \right), \text{ and} \tag{3.9a}$$

$$\sigma_r = k(\bar{u} - c_r), \tag{3.9b}$$

where  $c = c_r + ic_i$  is the complex phase speed.

Equation (3.5) shows that the generation of eddy available potential energy is due to dust-modified baroclinic effects  $G_1|v||T|$  and dust-modified available potential energy  $G_2|T|^2$ . The dust effects appear explicitly in the coefficients  $G_1$  and  $G_2$  and implicitly in the eddy correlations  $|v||T|$  and  $|T|^2$ . It is conceivable that the eddy correlations could depend on the dust field in a way that offsets the dust dependence seen in the coefficients multiplying them. In this situation the dust would have

little effect on  $\overline{\text{GE}}$ . To determine if this is the case would require solving for the eddy fields, a formidable if not impossible task for realistic background flows. We can make analytical progress, however, if we assume, consistent with our numerical results, that the dust diabatic heating rate  $\dot{q}$  is small but finite, say,  $O(\epsilon)$ , where  $\epsilon \ll 1$ , such that  $\dot{q} \rightarrow \epsilon \dot{q}$ . We can then expand the eddy fields in a Taylor series about  $\epsilon \dot{q} \ll 1$  to obtain for the meridional velocity field  $v(\mathbf{x}, p; \epsilon \dot{q}) \approx v(\mathbf{x}, p; 0) + O(\epsilon \dot{q})$  (other eddy fields will have the same form). Insertion of this expression and a similar one for temperature into (3.5) shows that to lowest order  $\overline{\text{GE}}$  is controlled by the dust physics in  $G_1$  and  $G_2$ .

Both  $G_1$  and  $G_2$  are functions of the dust sedimentation rate  $D$ , which is always stabilizing; that is, as  $D$  and thus  $\sigma_i$  increase,  $\overline{\text{GE}}$  is reduced. The baroclinic coefficient  $G_1$  is also a function of the dust radiative feedbacks  $\alpha_y$  and  $\alpha_p$ , which originate from the meridional and vertical advection of the zonal-mean dust by the eddy wind field [see (3.2)]. Because  $A(y, p; \bar{\gamma}) > 0$ , the signs of  $\alpha_y$  and  $\alpha_p$  are determined by the spatial gradients of the zonal-mean dust distribution. At locations where the zonal-mean concentration is maximized,  $\alpha_y$  and  $\alpha_p$  vanish and, consequently, the dust has no effect on  $\overline{\text{GE}}$ . Depending on the dust distribution, the effects of  $\alpha_y$  and  $\alpha_p$  may augment or oppose each other. Because  $\alpha_p$  is modulated by the vertical shear, as seen in (3.6a), its influence on  $\overline{\text{GE}}$  is largest near the AEJ.

For our representative AEJ and dust distribution shown in Figs. 1 and 2, our numerical integrations show

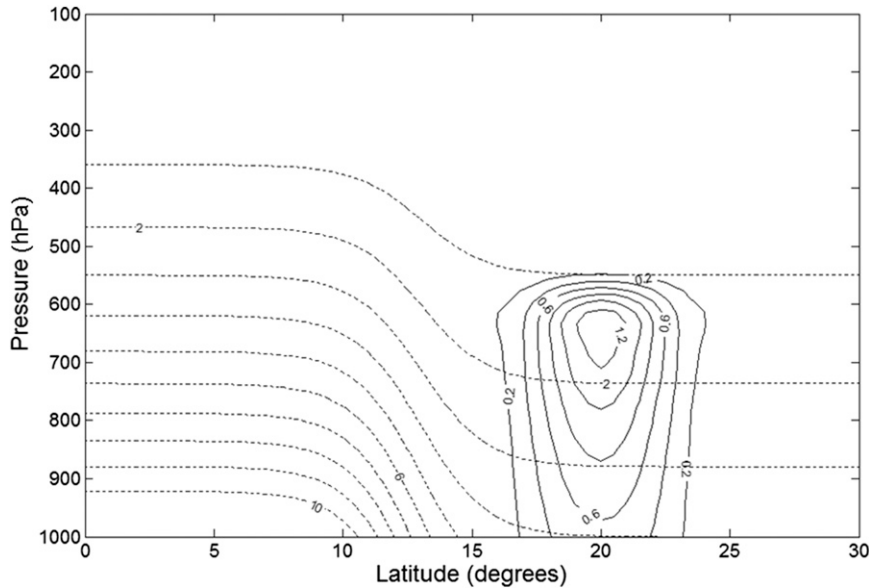


FIG. 3. Total dust-heating rate (solid) and reference water vapor profile (dotted). The dust-heating rate is computed for a declination angle of  $15^\circ$  and solar zenith angle of  $30.5^\circ$ . Contour intervals are  $0.2 \text{ K day}^{-1}$  and  $1.0 \text{ g kg}^{-1}$  for the heating rate and water vapor, respectively. The maximum dust-heating rate is  $\sim 1.2 \text{ K day}^{-1}$  at 650 hPa and  $20^\circ\text{N}$ .

that  $\alpha_y$  generally dominates over  $(pf/R)(\partial\bar{u}/\partial p)\alpha_p$ . In this case the baroclinic term in (3.6a) can be approximated as

$$G_1|v||T| \approx C\sigma_r\alpha_y|v||T|. \quad (3.10)$$

Consider the region south of the dust maximum ( $\leq 20^\circ\text{N}$ ) and below the jet maximum ( $\geq 650 \text{ hPa}$ ). In this region  $\alpha_y > 0$  as seen in Fig. 2, while  $|v||T| > 0$ . Consequently the dust-modified baroclinic term increases  $\overline{GE}$ . Because  $\overline{GE} \propto C$ , it is further increased in the vicinity of a critical surface, since  $C$  increases as  $\sigma_r \rightarrow 0$ .

The sign of the eddy available potential energy term  $G_2|T|^2$  in (3.5) is controlled by the dust coefficient  $G_2$  since  $|T|^2 > 0$ . Because the source of the dust is at the surface, the dust concentration is generally largest there and decreases with height, so that  $\alpha_p > 0$ . For the dust profile shown in Fig. 2,  $\alpha_p$  is zero in the boundary layer ( $\geq 650 \text{ hPa}$ ) and positive above. This  $\alpha_p$  vertical distribution means that the dust-modified eddy available potential energy decreases  $\overline{GE}$  near the jet.

#### 4. Numerical results

##### a. Experiments

Numerical experiments without dust (NODUST) and with dust (DUST) are run for zonal wavelengths spanning 2500–5000 km (zonal wavenumbers 8–16), which correspond to the wavelengths associated with observed

AEWs (Burpee 1975). For the NODUST experiments, the model parameterizations are deactivated in which case the dust is a passive tracer. For the DUST experiments, only the radiation parameterization is activated; this isolates the direct dust–radiative feedbacks on the model circulation.

For each experiment, a single wave is superimposed onto the basic state wind. The initial wave amplitude is small ( $10^{-5} \text{ m s}^{-1}$ ) and constant in the latitude–height plane. We use sufficiently small amplitudes to ensure linearity; that is, we require that the ratio of the wave amplitude to the maximum zonal-mean wind remains small, say  $O(\delta)$ , where we have chosen  $\delta \approx 0.05$ . As the model integrates forward in time, the waves in the horizontal wind fields generate waves for all of the other prognostic fields (vertical velocity, streamfunction, temperature, and dust). We continue to integrate the model until the domain average total perturbation wave energy (kinetic plus potential) grows exponentially to an accuracy of  $10^{-4}$  for at least 12 h. This typically occurs between 10 and 20 days of model integration. Once exponential growth is achieved, the various disturbance characteristics are calculated for the experiments presented below.

##### b. Growth rates, phase speeds, and structures

Figure 4 shows the growth rates and phase speeds as a function of zonal wavelength for the NODUST (solid) and DUST (dashed) experiments. For both

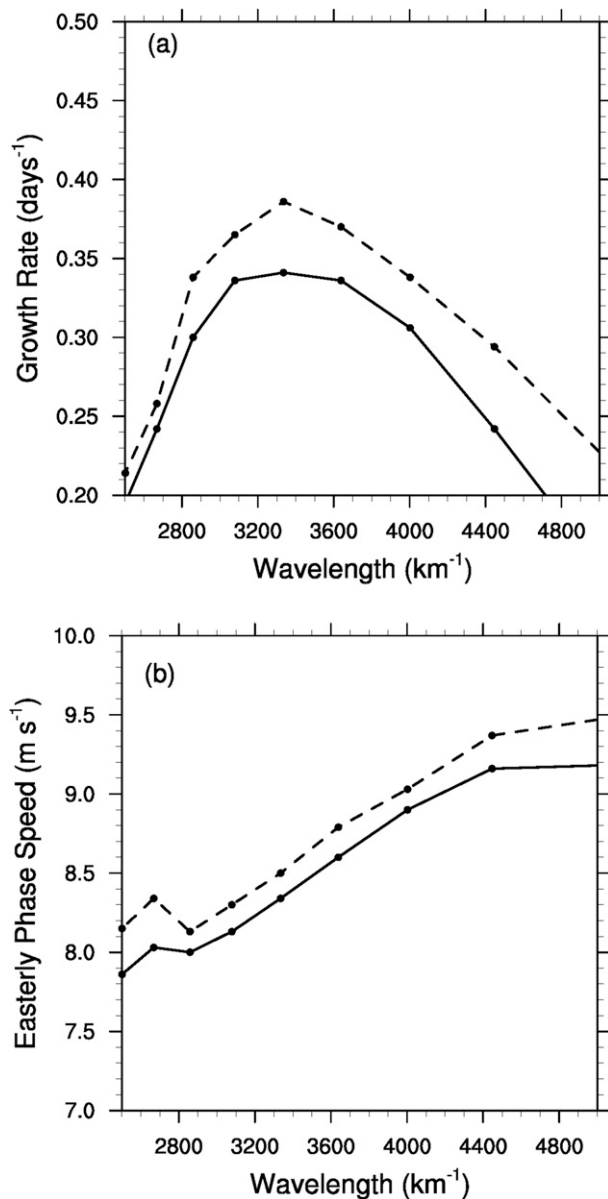


FIG. 4. (a) Growth rates and (b) easterly phase speeds for the NODUST (solid) and DUST (dashed) experiments.

experiments, growth rates peak at wavelengths between 3000 and 3500 km; the easterly phase speeds increase with increasing wavelength. The dust radiative effects increase the growth rate by  $\sim 5\%$ – $20\%$  (Fig. 4a) and the easterly phase speeds by  $\sim 1\%$ – $3\%$  (Fig. 4b). For both experiments, the fastest-growing AEW has a wavelength of 3300 km (zonal wavenumber 12); the dust radiative feedbacks increase its growth by  $\sim 15\%$ .

Figure 5 shows the horizontal structures for the fastest-growing AEW for the NODUST (left column) and DUST (right column) experiments. Plotted are the meridional wind (Figs. 5a,b) at 700 hPa and the

temperature (Figs. 5c,d) and vertical motion (Figs. 5e,f) at 850 hPa. Figures 5a and 5b show that for both the NODUST and DUST experiments the trough axis (bold line) tilts westward (eastward) with increasing latitude north (south) of the jet axis ( $15^\circ\text{N}$ ). This structural configuration corresponds to the convergence of momentum flux and thus barotropic instability. Figures 5c–f show that north of the AEJ axis ( $\sim 15^\circ$ – $18^\circ\text{N}$ ), warm anomalies (Figs. 5c,d) are collocated with low-level ascent (Figs. 5e,f) ahead of the trough. This correlation corresponds to baroclinic instability—that is, the conversion of eddy available potential energy to eddy kinetic energy. Although the figures show that the dust has no significant effect on the phasing between the wind, temperature, and vertical motion fields, there are significant changes to the amplitudes. For example, comparison of Figs. 5a and 5b shows that the dust increases the amplitude of the meridional wind by  $\sim 33\%$  north of the jet axis and decreases it by  $\sim 33\%$  south of the jet axis. Similar amplitude changes occur for the zonal wind velocities (not shown). These amplitude changes indicate that at 700 hPa the dust increases the momentum fluxes north of the AEJ axis and decreases them south of the AEJ axis.

Figure 6 shows the vertical structures for the fastest-growing AEW for the NODUST (left column) and DUST (right column) experiments. Plotted are the meridional wind (Figs. 6a,b), temperature (Figs. 6c,d) and vertical motion (Figs. 6e,f). The fields are displayed for  $18^\circ\text{N}$ , which is where the dust and the horizontal structures shown in Fig. 5 are large within the dust plume. Figures 6a and 6b show that below the AEJ maximum (650 hPa), the AEW trough tilts eastward with height, which, consistent with the positive correlations between the temperature and vertical motions fields shown in Fig. 5, is indicative of baroclinic instability in easterly flow. Comparison of Figs. 6a and 6b shows that the dust steepens the vertical tilt of the trough at midlevels and slightly lessens it at low levels. Also, the comparison of the temperature (Figs. 6c,d) and vertical motion (Figs. 6e,f) fields show that dust-modified wave amplitudes are stronger at midlevels and weaker at low levels. These dust-induced changes increase the baroclinic instability at midlevels and decrease at low levels.

### c. Global and local energetics

Figure 7 shows, for the NODUST and DUST experiments, the domain-averaged energy conversions<sup>3</sup> for

<sup>3</sup>The mathematical expressions for the energy conversions can be found in Norquist et al. (1977).

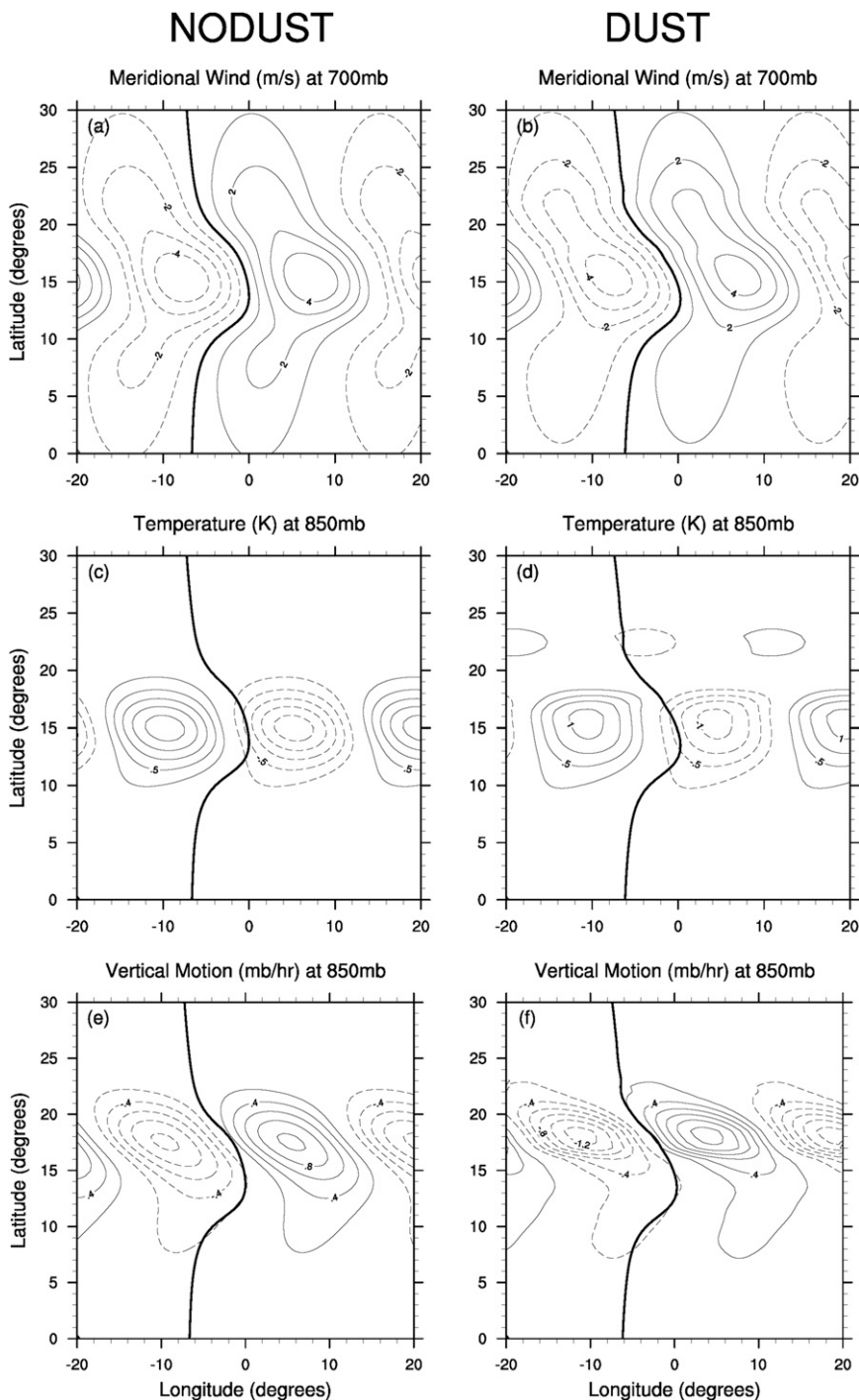


FIG. 5. Horizontal structures for the fastest-growing AEW for (left) the NODUST experiments and (right) the DUST experiments. (a),(b) Meridional velocity at 700 hPa; (c),(d) temperature at 850 hPa; and (e),(f) vertical motion at 850 hPa. Also shown is the AEW trough at 700 hPa (thick line). All wave fields are scaled to produce a meridional velocity of  $5 \text{ m s}^{-1}$ . Solid and dashed contours denote positive and negative values, respectively. Contour intervals are  $1.0 \text{ m s}^{-1}$  in (a) and (b);  $0.25 \text{ K}$  in (c) and (d); and  $0.2 \text{ hPa h}^{-1}$  in (e) and (f).

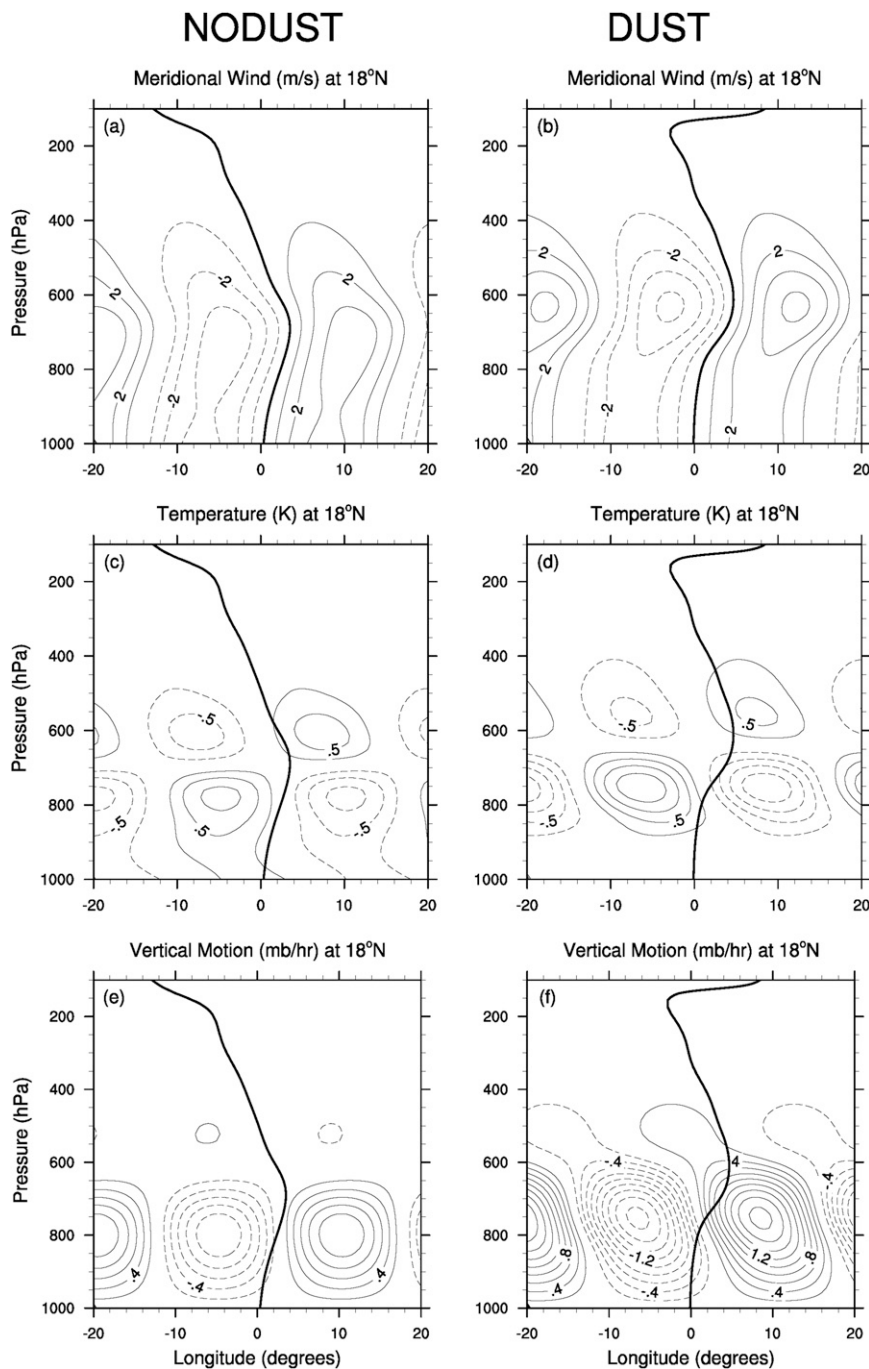


FIG. 6. Vertical structures of the wave fields shown in Fig. 5 at 18°N. Also shown is the AEW trough (bold).

the fastest-growing AEW. For both experiments the domain-averaged barotropic energy conversion  $\langle CK \rangle$  dominates over the domain-averaged baroclinic energy conversion  $\langle CE \rangle$ . This is consistent with previous dust-free linear studies (see Table 2). The ratio of baroclinic to barotropic energy conversion  $\langle CE \rangle / \langle CK \rangle$  is 0.09, which is  $\sim 22\%$  larger in the DUST experiment. The

dust-induced increase in  $\langle CE \rangle / \langle CK \rangle$  is mainly due to the  $\sim 40\%$  ( $\sim 0.02 \text{ W m}^{-2}$ ) increase in  $\langle CE \rangle$  versus a  $\sim 10\%$  ( $\sim 0.05 \text{ W m}^{-2}$ ) increase in  $\langle CK \rangle$ . The increase in  $\langle CE \rangle$  originates from the domain-averaged generation of available perturbation energy by the dust field  $\langle GE \rangle$ , since there is no significant change in the conversions of zonal to eddy available potential energy  $\langle CA \rangle$ .

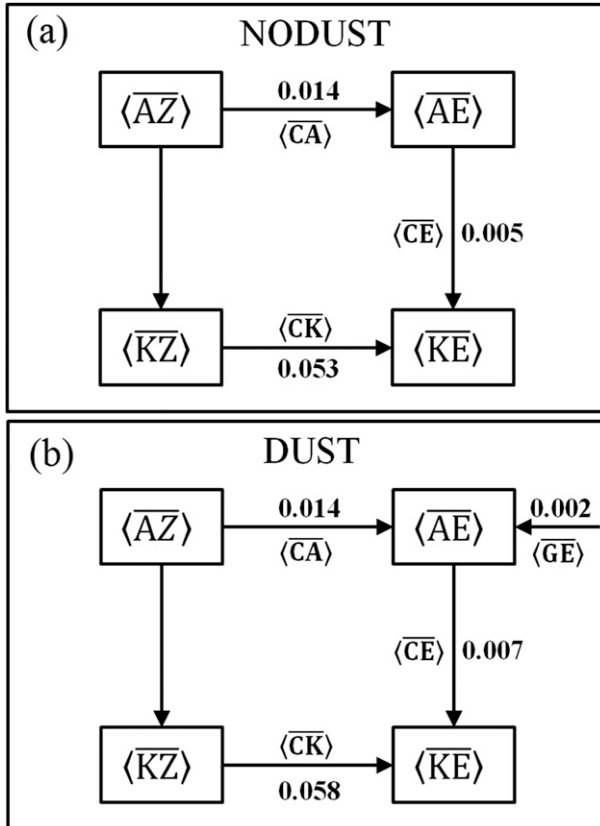


FIG. 7. Domain-averaged energetics for the fastest-growing wave for the (a) NODUST and (b) DUST experiments. Terms are  $\langle \overline{AZ} \rangle$ , zonal available potential energy;  $\langle \overline{KZ} \rangle$ , zonal kinetic energy;  $\langle \overline{AE} \rangle$ , eddy available potential energy; and  $\langle \overline{KE} \rangle$ , eddy kinetic energy. Energy conversion terms for the perturbation ( $\text{W m}^{-2}$ ) are  $\langle \overline{CA} \rangle$ , conversion of  $\langle \overline{AZ} \rangle$  to  $\langle \overline{AE} \rangle$ ;  $\langle \overline{CE} \rangle$ , baroclinic energy conversion;  $\langle \overline{CK} \rangle$ , barotropic energy conversion; and  $\langle \overline{GE} \rangle$ , generation of  $\langle \overline{AE} \rangle$  due to direct dust radiative feedbacks.

Figures 8–10 show latitude–height cross sections of the local (in  $y$  and  $p$ ) zonally averaged eddy kinetic energy per unit mass  $\overline{KE}$ , barotropic energy conversion  $\overline{CK}$ , and baroclinic energy conversion  $\overline{CE}$ . These energy fields are commonly used to diagnose AEWs in the absence of dust (e.g., Thorncroft and Hoskins 1994; Paradis et al. 1995).

For the NODUST and DUST experiments, Figs. 8a and 8b show that the  $\overline{KE}$  has two midlevel maxima that flank either side of the AEJ axis, with the northern flank extending to the surface. In the NODUST experiment, the  $\overline{KE}$  distribution is consistent with Thorncroft and Hoskins (1994) and Paradis et al. (1995). Comparison of Figs. 8a and 8b shows that the dust increases the  $\overline{KE}$  north of the jet axis (solid line). In this region, the dust increases the maximum  $\overline{KE}$  by  $\sim 33\%$ , while the region of large  $\overline{KE}$ , as measured by the  $\overline{KE} = 8 \text{ m}^2 \text{ s}^{-2}$  contour, vertically expands by  $\sim 50 \text{ hPa}$  and meridionally

contracts by  $\sim 1^\circ$ . The increase in the maximum  $\overline{KE}$  is due to a  $\sim 2 \text{ m}^2 \text{ s}^{-2}$  increase in dust-modified  $\overline{KE}$  between  $\sim 17^\circ$  and  $20^\circ \text{N}$  and  $\sim 600$  and  $800 \text{ hPa}$  (see Fig. 8c). South of this region ( $\sim 10^\circ$ – $17^\circ \text{N}$  and  $\sim 600$ – $800 \text{ hPa}$ ) the difference between the NODUST and DUST experiments (Fig. 8c) shows two  $\sim 2$ – $4 \text{ m}^2 \text{ s}^{-2}$  vertical dipoles in  $\overline{KE}$  (positive over negative). The differences between the NODUST and DUST experiments shown in Fig. 8c indicate that the dust–radiative feedbacks vertically expand the  $\overline{KE}$  distribution by as much as  $\sim 50 \text{ hPa}$  and meridionally contract it by  $\sim 1^\circ$  below  $\sim 700 \text{ hPa}$ .

Similar to  $\overline{KE}$ , the local time rate of change in kinetic energy due to barotropic processes  $\overline{CK}$ , which is shown in Figs. 9a and 9b, possesses two midlevel maxima that flank the jet. For the NODUST experiment, the structure of  $\overline{CK}$  is consistent with Paradis et al. (1995); that is,  $\overline{CK}$  has maxima north and south of the jet, though it is about twice as large north of the jet. For the DUST experiment, the dust-induced changes in  $\overline{CK}$  are largest north of the AEJ axis, which is consistent with the dust-induced changes in  $\overline{KE}$  shown in Fig. 8b. For example, the dust increases the maximum in  $\overline{CK}$  by  $\sim 50\%$  north of the AEJ axis, which is coincident with the maximum in  $\overline{KE}$  at  $\sim 18^\circ \text{N}$  and  $\sim 750 \text{ hPa}$ . Dust also increases  $\overline{CK}$  by  $\sim 10\%$ – $50\%$  between  $\sim 17^\circ$  and  $21^\circ \text{N}$  and  $\sim 700$  and  $500 \text{ hPa}$ , which encompasses the region where the dust expands the  $\overline{KE}$  vertically. South of this region ( $\sim 15^\circ$ – $17^\circ \text{N}$ ), the difference in  $\overline{CK}$  between the NODUST and DUST experiments shows a vertical dipole structure (see Fig. 9c), which is consistent with the dust-induced meridional contraction in  $\overline{KE}$  (see Fig. 8c). In contrast to  $\overline{KE}$ , however, the vertical dipole in  $\overline{CK}$  (see Fig. 9c) does not extend south of the AEJ.

Figures 10a and 10b show that the local time rate of change in the kinetic energy due to baroclinic processes  $\overline{CE}$  has a single maximum north of the AEJ axis. In the NODUST experiment, the structure of  $\overline{CE}$  is consistent with Paradis et al. (1995), though the magnitudes of  $\overline{CE}$  are  $\sim 33\%$  lower in our study. The lower magnitudes in  $\overline{CE}$  are expected since  $\langle \overline{CE} \rangle / \langle \overline{CK} \rangle$  is also lower in our study (see Table 2). For the DUST experiment, Fig. 10b shows that the dust increases the maximum in  $\overline{CE}$  by  $\sim 100\%$  and shifts it vertically by  $\sim 50 \text{ hPa}$  and north by  $\sim 1^\circ$ . The maximum in  $\overline{CE}$  is coincident with the maximums in both  $\overline{KE}$  (see Fig. 8b) and  $\overline{CK}$  (see Fig. 9b). Figure 10c shows that in the region of largest  $\overline{CE}$  ( $\sim 18^\circ \text{N}$  and  $\sim 750 \text{ hPa}$ ), the difference in  $\overline{CE}$  between the NODUST and DUST experiments is about the same as the difference in  $\overline{CK}$  shown in Fig. 9c. As a result, the collocation of the dust-induced maxima in  $\overline{CE}$  and  $\overline{CK}$  yields, locally,  $\overline{CE} / \overline{CK} = 0.41$ , which is about a factor of 4 larger than the globally averaged ratio,  $\langle \overline{CE} \rangle / \langle \overline{CK} \rangle$ .

TABLE 2. Listed are the characteristics of the fastest-growing AEWs for the select studies in Table 1 and for the NODUST and DUST experiments in this study. In the last column,  $\langle \overline{CE} \rangle / \langle \overline{CK} \rangle$  is the ratio of the domain-averaged baroclinic to barotropic energy conversion; the negative ratio in the Kwon (1989) study is because  $\langle \overline{CE} \rangle < 0$ .

Reference	AEW characteristics			
	Growth rate ( $\text{day}^{-1}$ )	Phase speed ( $\text{m s}^{-1}$ )	Wavelength (km)	$\langle \overline{CE} \rangle / \langle \overline{CK} \rangle$
Rennick (1976)	0.37	15.8	3000	0.20
Kwon (1989)	0.39	6.6	3100	-0.26
Thornicroft and Hoskins (1994)	0.28	8.4	3500	0.19
Paradis et al. (1995)	0.40	7.64	3300	0.21
Hall et al. (2006)	0.47	7.07	2980	2.16
Current study: NODUST	0.34	8.34	3300	0.07
Current study: DUST	0.39	8.44	3300	0.09
Range	0.28–0.47	6.6–15.8	2980–3500	From -0.26 to 2.16

The dust radiative feedbacks produce a vertical dipole in the  $\overline{CE}$  difference that extends south of the AEJ axis (see Fig. 10c), but the dipole is  $\sim 50$  hPa lower than those shown in the difference plots for  $\overline{KE}$  (Fig. 8c) and  $\overline{CK}$  (Fig. 9c).

The local energetics analysis discussed above shows that all of the dust-modified energy conversions are largest between the jet axis and the maximum in the dust concentration. This can be explained using the analytical analysis presented in section 3. Recall from (3.5)–(3.9), the dust physics that controls the generation of eddy available potential energy  $\overline{GE}$  is embodied in two dust feedback terms  $\alpha_y$  and  $\alpha_p$ , which are proportional to the meridional and vertical gradients of the basic state dust field, respectively. Moreover, both dust feedback terms are modulated by the Doppler-shifted frequency  $\sigma_r$ , whereas only  $\alpha_p$  is modulated by the vertical shear of the jet. Our numerical experiments show that  $\alpha_y$  and  $\alpha_p$  both contribute to  $\overline{GE}$ , but  $\alpha_y$  generally dominates over  $\alpha_p$  by about a factor of 3 in the growth rate calculation. If we then assume that  $\alpha_y$  is the primary control of  $\overline{GE}$ , (3.10) shows  $\overline{GE}$  is largest where the product of the heat flux and meridional gradient of the dust is largest and the Doppler-shifted frequency vanishes. This is confirmed in Fig. 11a, which shows  $-|v||T|\partial\overline{\gamma}/\partial y$  (thin contours) and the critical surface along which  $\sigma_r$  vanishes (bold line). The figure shows that  $-|v||T|\partial\overline{\gamma}/\partial y$  is largest where  $\sigma_r = 0$  ( $\sim 18^\circ\text{N}$  and  $\sim 750$  hPa), which is precisely the location where the model generated  $\overline{GE}$  shown in Fig. 11b is maximized, in agreement with the prediction of the analytical analysis.

#### d. Eliassen–Palm flux diagnostics

Eliassen–Palm (EP) fluxes can be used to understand how waves feedback on the zonal-mean flow. Following Edmon et al. (1980), the EP flux vector components in spherical geometry can be written as

$$\mathbf{F} = [F_{(\phi)}, F_{(p)}] = r_E \left[ -\cos(\phi)\overline{uv}, \frac{f}{\partial\theta/\partial p} \cos(\phi)\overline{v\theta} \right], \quad (4.1)$$

where  $r_E$  is the radius of Earth and  $\phi$  is latitude (degrees); all other variables are defined in section 3.

Figure 12 shows the EP flux vectors (arrows) and divergences (contours) for the fastest-growing wave for the NODUST and DUST experiments. For both experiments, the EP flux vectors generally point away from the AEJ core. For example, north (south) of the jet,  $\mathbf{F}$  indicates a northward (southward) flux of easterly momentum, while below the jet there is an equatorward heat flux. Consequently, the momentum and heat fluxes together reduce the horizontal and vertical shear of the jet, consistent with the energetics of the amplifying wave discussed in section 4c.

For the NODUST and DUST experiments the EP flux divergence  $\nabla \cdot \mathbf{F}$  is characterized by a divergent region (solid contours) surrounding the jet core and two convergent regions (dotted contours) on its flanks. For the NODUST experiment (Fig. 12a),  $\nabla \cdot \mathbf{F}$  is asymmetric about the jet, which is consistent with the asymmetry in the barotropic energy conversions shown in Fig. 9a, an asymmetry that is consistent with wave driving that reduces the horizontal shear on both sides of the jet. For the DUST experiment (Fig. 12b),  $\nabla \cdot \mathbf{F}$  increases by  $\sim 50\%$ – $100\%$  north of the jet and decreases by  $\sim 0\%$ – $50\%$  south of the jet. Thus, the dust-modified wave driving further reduces the shear north of the jet, producing greater lateral asymmetry in the jet. Like the energetics, the dust-modified  $\nabla \cdot \mathbf{F}$  is largest between the jet axis at  $15^\circ\text{N}$  and the dust maximum at  $20^\circ\text{N}$ .

#### e. Sensitivity to AOD and plume location

The results presented above are based on a dust plume whose location, structure, and concentration are consistent with observations. These dust plume characteristics, however, may be quite variable (Karyampudi

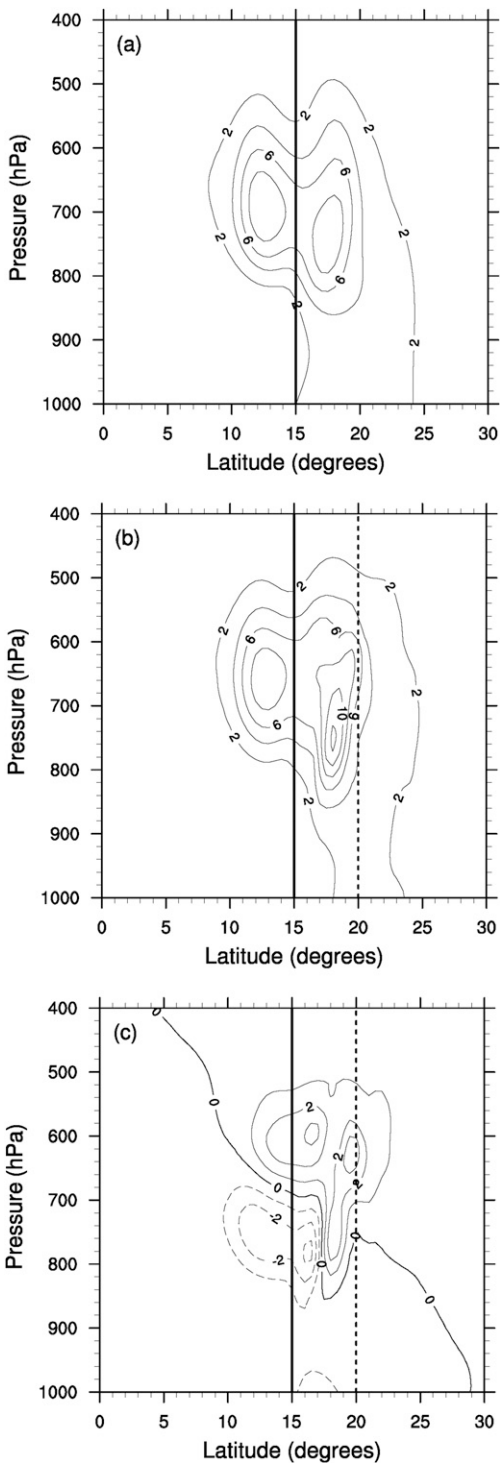


FIG. 8. The  $\overline{KE}$  for the fastest-growing AEW for the (a) NODUST experiment and (b) DUST experiment and for (c) the difference between the two. Contour spacings are  $2.0 \text{ m}^2 \text{ s}^{-2}$  in (a) and (b) and  $1.0 \text{ m}^2 \text{ s}^{-2}$  in (c). Positive values (solid) in (c) correspond to increases in  $\overline{KE}$  for the DUST experiment. Also shown are the latitude of the jet axis (solid vertical line) and the latitude of the maximum dust concentration (dotted vertical line).

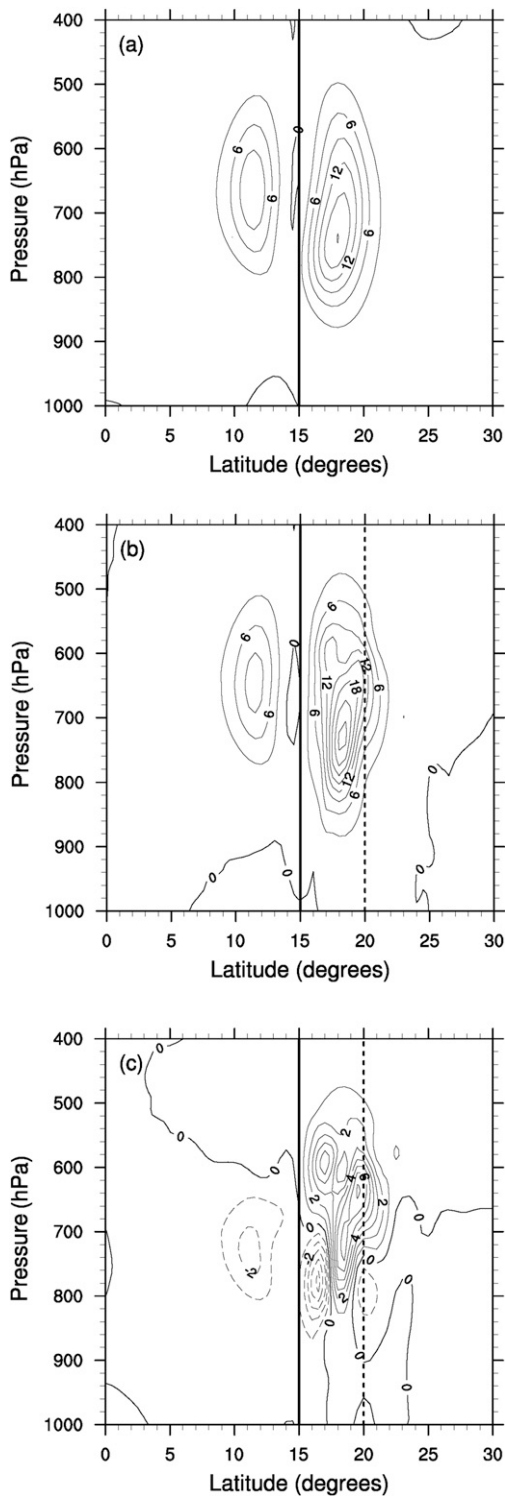


FIG. 9. As in Fig. 8, but for  $\overline{CK}$ . Contour spacings are  $3.0 \times 10^{-6} \text{ W m}^{-2} (\text{pa m})^{-1}$  in (a) and (b) and  $1.0 \times 10^{-6} \text{ W m}^{-2} (\text{pa m})^{-1}$  in (c).

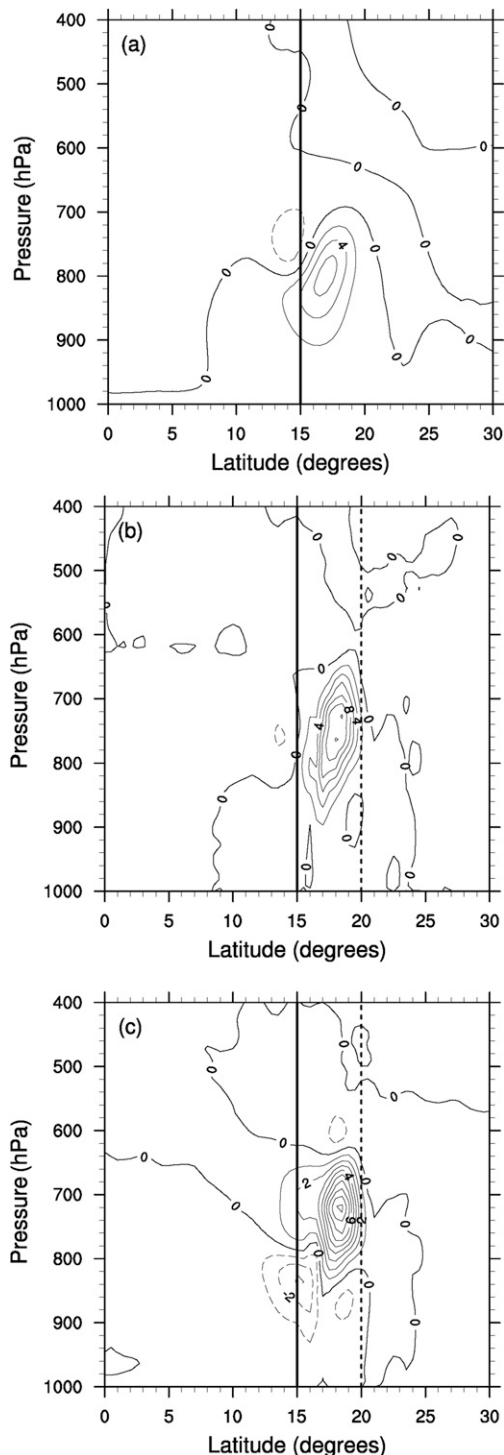


FIG. 10. As in Fig. 8, but for  $\overline{GE}$ . Contour spacings are  $2.0 \times 10^{-6} \text{ W m}^{-2} (\text{pa m})^{-1}$  in (a) and (b) and  $1.0 \times 10^{-6} \text{ W m}^{-2} (\text{pa m})^{-1}$  in (c).

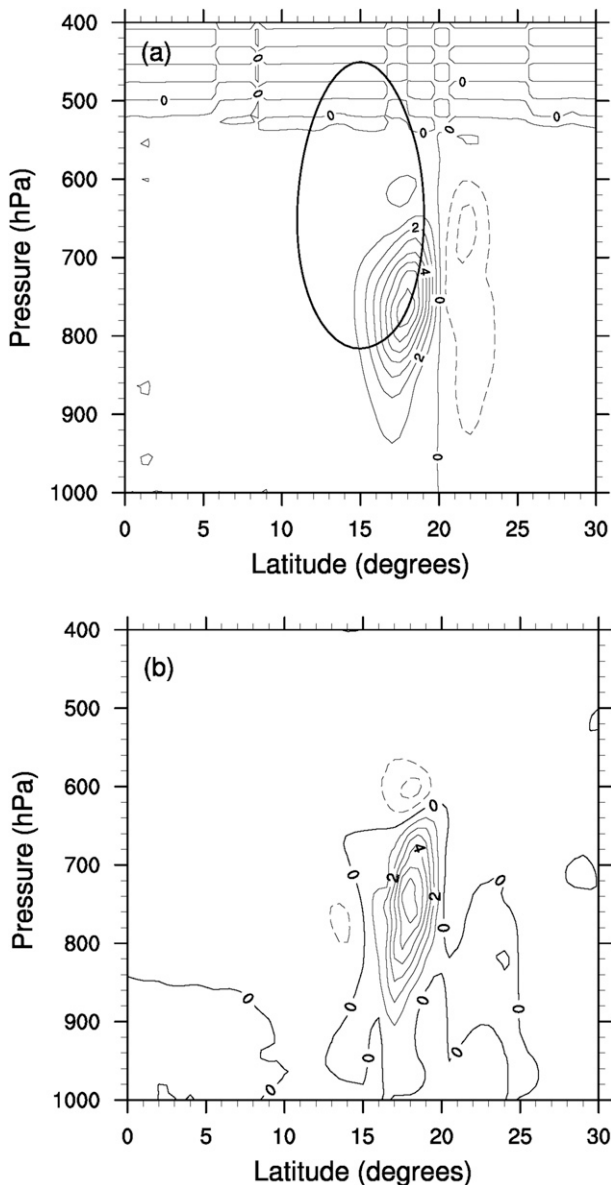


FIG. 11. (a) Plotted is  $-|v||T|\partial\overline{\gamma}/\partial y$  (thin contours) and the critical surface along which  $\sigma_r$  vanishes (thick curve). When the meridional advection of dust dominates over the vertical advection, these quantities together control  $\overline{GE}$  [see section 3 and (3.10)]; the contour interval is  $1.0 \times 10^{-13} \text{ K s}^{-1}$ . (b) Model generated  $\overline{GE}$  for the fastest-growing AEW; the contour interval is  $1.0 \times 10^{-6} \text{ W m}^{-2} (\text{pa m})^{-1}$ .

et al. 1999). Thus we have carried out some additional experiments to determine the sensitivity of the growth rates to 1) different maximum AODs ( $\tau$ ) and 2) different locations of the plume relative to the jet. The AODs were chosen to range from  $\tau = 0$  to  $\tau = 2.5$ , although AODs as large as  $\tau = 4.0$  are often observed over North Africa (Kocha et al. 2012). We do not consider AODs  $> 2.5$ , since doing so would violate our modeling

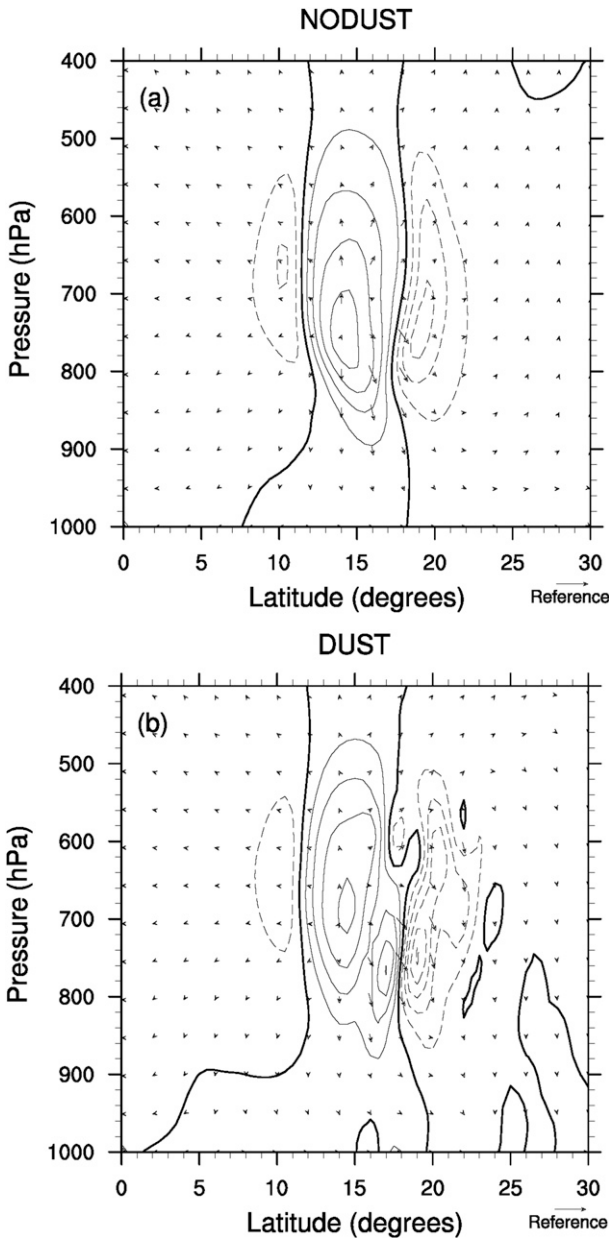


FIG. 12. EP flux vectors (arrows) and EP flux divergence/convergence (solid/dashed) for the fastest-growing AEW for the (a) NODUST experiment and (b) DUST experiment. The vertical component of the EP vectors is scaled up in the figure; the length of the EP reference vector below each figure is  $1 \times 10^{14} \text{ m}^3 \text{ (rad)}$  for the horizontal component and  $2 \times 10^{17} \text{ m}^3 \text{ (pa)}$  for the vertical component. The contour interval is  $1 \times 10^{15} \text{ m}^3$ .

assumption that the ratio of dust-induced diabatic divergences to the relative vorticity remain small, an assumption that allows us to fix our basic states rather than adjust them for different dust distributions (see section 2a). Figure 13 shows that for the dust structure shown in Fig. 2, the growth rate of the fastest-growing AEW increases monotonically with AOD. The growth rates for

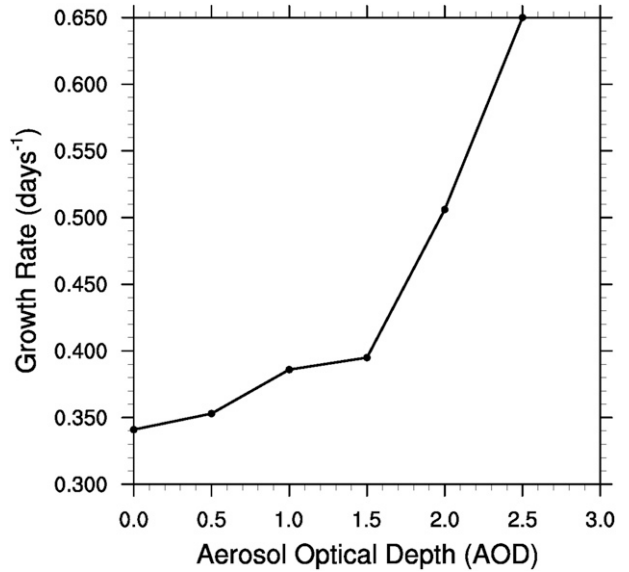


FIG. 13. Linear growth rate of the fastest-growing AEW as a function of the maximum AOD for the dust plume shown in Fig. 2.

$\tau = 0.5$ ,  $\tau = 1.0$ ,  $\tau = 2.0$ , and  $\tau = 2.5$  are about 3%, 15%, 48%, and 90% larger than the NODUST experiment.

The numerical results presented in sections 4b–4d were based on a plume centered at 20°N. Figure 14 shows the growth rate of the fastest-growing AEW for plumes centered at different latitudes north of the AEJ axis, ranging from 18° to 22°N. This latitude range is home to the major dust source emission regions over North Africa (Engelstaedter and Washington 2007). Figure 14 shows that when the plume is located at 21°N the growth rate is maximized; the growth rate at 21°N is ~2% larger than the growth rate at 20°N. Beyond 21°N, the growth rate rapidly decreases monotonically, consistent with our analytical analysis. Specifically, as the plume is shifted beyond 21°N, the maximum in the basic state meridional dust gradient is shifted away from the critical surface (Fig. 11a; bold), which reduces the maximum in  $\overline{GE}$ . As the plume is shifted south of 21°N, the growth rate also decreases, though the decrease is nonmonotonic. This nonmonotonic decrease in the growth rate is due to the change in the relative contributions of  $\alpha_y$  and  $\alpha_p$  as the plume approaches the jet core, where, recall from (3.6a),  $\alpha_p$  is modulated by the vertical shear.

### 5. Summary and conclusions

African easterly waves and the episodic formation of vast plumes of Saharan mineral dust aerosols are among the most important atmospheric circulation

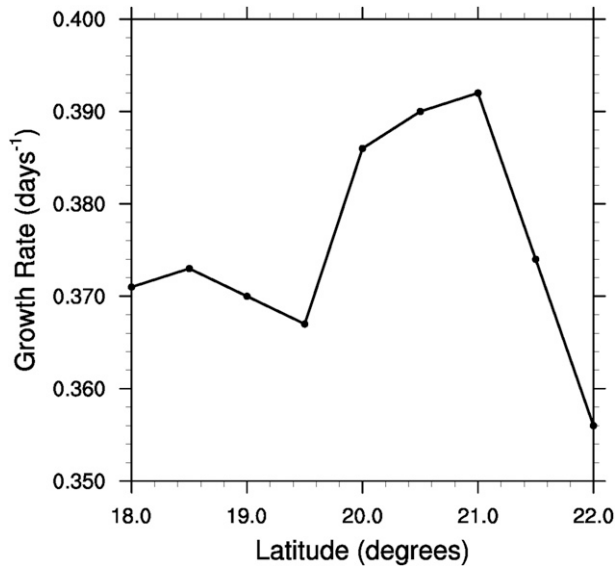


FIG. 14. The linear growth rate of the fastest-growing AEW as a function of the central latitude for the dust plume distribution shown in Fig. 2.

features over North Africa. The AEWs are often involved in the formation of Atlantic hurricanes (Landsea 1993), while the dust plumes alter the radiative heating of the atmosphere (Carlson and Benjamin 1980). Studies show that the AEWs often play a role in the formation of the plumes (Knippertz and Todd 2010). But as discussed in the introduction, the effects of Saharan dust on AEWs have produced contradictory results. For example, some studies find that the dust strengthens the AEWs (Jones et al. 2004; Lavaysse et al. 2011; Ma et al. 2012) while others find that the dust weakens the AEWs (Karyampudi and Carlson 1988; Reale et al. 2009; Jury and Santiago 2010; Ismail et al. 2010). A recent study finds that the dust may strengthen or weaken the growth of the AEWs depending on the position of the AEWs relative to the dust field (Hosseinpour and Wilcox 2014). Most of these studies, however, have focused on the eastern Atlantic, a region far from the North African origin of both the AEWs and dust plumes. Moreover, the studies have neither explicitly identified the dust physics that affects the AEWs nor carried out detailed calculations on how the dust physics affects the linear dynamics of the AEWs.

To identify the dust physics that affects the AEWs, we have combined the thermodynamic equation and a dust continuity equation to obtain an analytical expression for the generation of eddy available potential energy by the dust field  $\overline{GE}$ . The dust-modified  $\overline{GE}$  is due to the advection of the basic state dust field by the waves, which involves the interaction between the wind,

temperature, and dust fields. The meridional and vertical advection of the dust may augment or oppose each other, depending on the spatial distribution of the dust field. The wave–dust advection is a function of the dust transmissivity, the spatial gradients of the dust field, and the Doppler-shifted frequency. For a given dust transmissivity, we show that the effects of dust on the linear dynamics of AEWs will be strongest in regions where the spatial gradients of dust are largest and where the Doppler-shifted frequency vanishes. Because the analytical expression for  $\overline{GE}$  explains our numerical results,  $\overline{GE}$  can be used as a tool for predicting the dust distributions that would have the strongest effects on the linear dynamics of AEWs.

The dust-modified growth, propagation, structure, energetics, and Eliassen–Palm fluxes of the model AEWs were calculated using a linearized version of the Weather Research and Forecasting Model coupled to an online dust model. Climatological distributions of the zonally averaged basic state wind and potential temperature were used for the calculations. Consistent with observations, the basic state dust plume was chosen Gaussian in the meridional direction, constant through the boundary layer and decreasing above. An aerosol optical depth of  $\tau = 1.0$ , which is a modest value based on observed plumes over North Africa, characterized the dust concentration for our comprehensive analysis. The results show the following:

- Dust–radiative feedbacks increase the growth rates of the modeled AEWs by  $\sim 5\%$ – $20\%$ . For the fastest-growing AEW (zonal wavenumber 12; zonal wavelength  $\sim 3300$  km), the growth rate increases by  $\sim 15\%$ . The easterly phase speeds for the AEWs increase from 1% to 3%.
- Dust–radiative feedbacks increase the local maximum barotropic and baroclinic energy conversions by  $\sim 50\%$  and  $\sim 100\%$ , respectively. The dust-modified local energetics is largest between the AEJ core ( $15^\circ\text{N}$ ) and the latitude of the dust maximum ( $20^\circ\text{N}$ ). At this location the maximum mean meridional dust gradient is coincident with the critical surface, consistent with the prediction obtained from our analytical analysis.
- Dust–radiative feedbacks increase the divergence of EP flux by  $\sim 50\%$ – $100\%$  between the AEJ core ( $15^\circ\text{N}$ ) and the latitude of the dust maximum ( $20^\circ\text{N}$ ). Thus, the dust enhances the shear reduction north of the jet axis.

To determine the sensitivity of the results, additional calculations were carried out for different locations of the dust plume relative to the AEJ and for different AODs. The calculations show that the results obtained

for our representative plume are indeed robust. Specifically, the growth rates are reduced when the plume is shifted away from the critical surface. The reductions in the growth rates are offset by increasing the AOD. For example, for  $\tau = 1.0$  the growth rate of the fastest-growing wave increases by  $\sim 15\%$  over the dust-free case, whereas for  $\tau = 2.5$ , which is still a modest value based on observed dust events over North Africa, the growth increases by  $\sim 90\%$  over the dust-free case.

The above results may provide some insights into the contradictory and sometimes inconclusive results found in previous studies of the interactions between Saharan dust and AEWs. In this study, we have focused on the dust–radiative heating profiles consistent with arid North Africa, where the AEWs and dust plumes both originate. In this region, the dust is well mixed in the boundary layer and sharply decreases above. Previous studies have focused on the eastern Atlantic, where the dust plumes are lofted above the cool, moist marine layer to form the SAL. Consequently, the dust concentrations increase with height in the lower troposphere and then decrease with height above. Our results show that the vertical distribution of the dust, specifically its sign and proximity to the jet, determines whether it alone increases or decreases the local generation of eddy available potential energy [see (3.5)–(3.9)]. Thus the difference between the vertical dust distribution over North Africa versus the eastern Atlantic may explain, in part, why the results we obtained for North Africa are more robust than those obtained in previous studies for the eastern Atlantic. A more complete comparison between the two regions, however, will also require knowledge of the meridional dust distribution, which we have shown generally plays the dominant role over North Africa. What role it plays over the eastern Atlantic is unclear.

Another possible reason for the contradictory results obtained in previous studies may be associated with the stage of development of the AEWs. In this study, we have focused on the incipient (linear) dynamics of AEWs. A scenario for the evolution of AEWs would begin with its incipient stage over North Africa, followed by its continued growth and westward movement, and eventual equilibration at finite amplitude over West Africa and the eastern Atlantic. It is conceivable that by the time the AEWs reach the eastern Atlantic, the AEW dynamics may be less sensitive to dust–radiative feedbacks owing to reduced concentrations in the dust field or less favorable dust distributions. Though this is a possibility, it is mitigated in part by [Chen et al. \(2015\)](#), who found that accounting for direct dust–radiative heating over the eastern Atlantic improved the forecast track of Hurricane Helene. Why the dust feedbacks would have a relatively robust effect on Helene and not

on AEWs in the same region clearly requires further study. We note, however, that [Chen et al. \(2015\)](#) did not include dust microphysics, which several studies have shown could play a role in tropical cyclogenesis (e.g., [Jenkins and Pratt 2008](#); [Jenkins et al. 2008](#)).

In this study, we have examined the linear stability of idealized zonal-mean basic states to dust-modified AEWs. Recent studies have examined the linear stability of realistic zonally varying basic states to dust-free AEWs ([Hall et al. 2006](#); [Leroux and Hall 2009](#)). For example, [Hall et al. \(2006\)](#) show that with realistic boundary layer damping a zonally varying jet is neutralized with respect to AEWs. Studies have shown, however, that other processes, such as convection, can maintain AEWs that would otherwise decay in the presence of realistic damping ([Mekonnen et al. 2006](#); [Thorncroft et al. 2008](#); [Berry and Thorncroft 2012](#)). For example, [Berry and Thorncroft \(2012\)](#) used the WRF Model to examine the effects of convection on the maintenance of an “average” AEW during September 2004. Using an energetics analysis, they showed that AEW growth depends on both adiabatic dynamical processes and diabatic convective processes. When the convection is turned off, they showed that the AEW weakens. Because we have demonstrated that dust radiative effects enhance the linear growth of the AEWs, it is plausible that the dust may also help generate and maintain AEWs in the presence of realistic damping in zonally varying flow.

*Acknowledgments.* The authors thank Emily Bercos-Hickey and William Turner IV for their comments on the manuscript. We also acknowledge high-performance computing support from Yellowstone (ark:/85065/d7wd3xhc) provided by NCAR’s Computational and Information Systems Laboratory. This work is supported by NSF Grant 1321720.

## APPENDIX A

### Basic States

The basic state zonal wind, potential temperature, dust mass mixing ratio, and reference water vapor are represented by the following analytical forms, respectively:

$$\bar{u}(\phi, \sigma) = a_1 \exp \left[ -\frac{(\phi - \phi_{\text{jet}})^2}{2b_1} - \frac{(\sigma - \sigma_{\text{jet}})^2}{2c_1} \right] \times \left[ 1 + \operatorname{erf} \left( \frac{\sigma - \sigma_{\text{jet}}}{2c_1} \right) \right], \quad (\text{A.1})$$

$$\bar{\theta}(\phi, \sigma) = \left\{ \begin{array}{ll} [T_s - a_2 \log(\sigma - \sigma_{\text{trop}})]\sigma^{-R/c_p} + \theta_e, & 1 \geq \sigma \geq \sigma_{\text{trop}} \\ \theta_T(\sigma_{\text{trop}} - \sigma) + \bar{\theta}_{\text{trop}} + \theta_e, & \sigma_{\text{trop}} > \sigma \end{array} \right\}, \quad (\text{A.2})$$

$$\bar{\gamma}(\phi, \sigma) = \left\{ \begin{array}{ll} a_3 \exp \left[ -\frac{(\phi - \phi_{\text{plume}})^2}{2b_3} \right] \tanh[c_3(\sigma - \sigma_{\text{plume}})], & 1 \geq \sigma \geq \sigma_{\text{plume}} \\ 0, & \sigma_{\text{plume}} > \sigma \end{array} \right\}, \quad \text{and} \quad (\text{A.3})$$

$$\bar{\eta}_r(\phi, \sigma) = -a_4 \left[ \tanh \left( \frac{\phi - \phi_q}{2b_4} \right) - c_4 \right] \left( \frac{\sigma}{\sigma_{\text{trop}}} \right)^2. \quad (\text{A.4})$$

In (A.1)–(A.4),  $\phi$  is latitude and  $\sigma$  is the vertical coordinate, where  $\sigma = 1$  at the surface and  $\sigma = 0$  at the model top. In (A.1)–(A.4),  $\sigma_{\text{jet}} = 0.65$  denotes the jet core,  $\sigma_{\text{trop}} = 0.15$  denotes the model tropopause, and  $\sigma_{\text{plume}} = 0.5$  denotes the top of the plume. All the other constants in (A.1)–(A.4) are listed in Table A1.

In (A.2) the two functions represent the potential temperature profiles for the troposphere and stratosphere. For both functions, thermal wind balance is assured by an appropriate choice of  $\theta_e(y, \sigma)$ , which is determined by solving a simplified version of the balanced equation presented in Wang (1995). In this study the basic state zonal wind is specified and there is no topography. If we assume that the effects of Earth's curvature and surface pressure gradients are small, the balanced equation can be written as

$$\frac{\partial^2 \Phi}{\partial \phi^2} = G - \frac{\bar{T}_r}{T_s} G_s, \quad \sigma \leq 1, \quad (\text{A.5})$$

where  $\Phi$  is the geopotential,  $\bar{T}_r(\sigma)$  is a reference temperature profile, subscript “s” denotes surface variables, and

$$G = f\xi - \bar{u}\beta. \quad (\text{A.6})$$

In (A.6),  $f$  is the Coriolis parameter,  $\beta$  is the meridional gradient of the Coriolis parameter, and  $\xi$  is the relative vorticity. Thus, the right-hand side of (A.5) is known. We solve (A.5) offline using successive overrelaxation at an accuracy  $O(10^{-5})$ . Once  $\Phi$  is obtained at all levels,  $\theta_e$  is calculated directly from

$$\theta_e = \left[ \frac{\partial \Phi}{\partial \sigma} \frac{p_s}{R(p_s - p_{\text{top}})} \right] \left( \frac{p}{p_s} \right)^{1-R/c_p}. \quad (\text{A.7})$$

## APPENDIX B

### Generation of Eddy Available Potential Energy by the Dust Field

The generation of eddy available potential energy is defined as  $\overline{\text{GE}} = (c_p \bar{S})^{-1} \bar{q} \bar{T}$  (Norquist et al. 1977). To derive an expression for  $\overline{\text{GE}}$  due to dust, we begin with the linearized temperature and dust mass mixing ratio [(3.1) and (3.2)]:

$$\left( \frac{\partial}{\partial t} + \bar{u} \frac{\partial}{\partial x} \right) T + v \frac{\partial \bar{T}}{\partial y} - \omega \bar{S} = \frac{A}{c_p} \gamma \quad \text{and} \quad (\text{B.1})$$

$$\left( \frac{\partial}{\partial t} + \bar{u} \frac{\partial}{\partial x} \right) \gamma + v \frac{\partial \bar{\gamma}}{\partial y} + \omega \frac{\partial \bar{\gamma}}{\partial p} = -D\gamma, \quad (\text{B.2})$$

where the expressions for the dust heating rate and sedimentation rate [(3.3) and (3.4)] have been used in (B.1) and (B.2). Solving (B.1) for the vertical motion  $\omega$  and inserting the result into (B.2) yields

$$\begin{aligned} & \left( \frac{\partial}{\partial t} + \bar{u} \frac{\partial}{\partial x} \right) \left( \gamma + \frac{1}{\bar{S}} \frac{\partial \bar{\gamma}}{\partial p} T \right) + \left( \frac{\partial \bar{\gamma}}{\partial y} + \frac{\partial \bar{T}}{\partial y} \frac{1}{\bar{S}} \frac{\partial \bar{\gamma}}{\partial p} \right) v \\ & + \left( D - \frac{A}{c_p} \right) \gamma = 0. \end{aligned} \quad (\text{B.3})$$

Normal mode solutions for  $v$ ,  $T$ , and  $\gamma$  are chosen of the form

$$\chi = |\chi| \exp[i(\varphi_\chi + \theta)] + \text{c.c.}, \quad (\text{B.4})$$

where  $|\chi(y, p)|$  and  $\varphi_\chi$  are the amplitude modulus and phase for a given variable;  $\theta(x, t) = k(x - ct)$ ,  $k$  is the zonal wavenumber, and  $c = c_r + ic_i$  is the (complex) phase speed; and c.c. denotes the complex conjugate of the preceding term. Using (B.4) for each of the eddy fields allows (B.3) to be written as

TABLE A1. Constants appearing in (A.1)–(A.4).

(A.1)	$a_1 = -13.25 \text{ m s}^{-1}$ , $b_1 = 3.75$ , $c_1 = 0.25$ , $\alpha_1 = -1.5$ , and $\phi_c = 15^\circ$
(A.2)	$a_2 = 91.2 \text{ K}$ , $T_s = 298.86 \text{ K}$ , $\theta_T = 475 \text{ K}$ , $\theta_{\text{trop}} = 356 \text{ K}$ , and $R/c_p = 0.286$
(A.3)	$a_3 = 18 \mu\text{g kg}^{-1}$ , $b_3 = 2$ , $c_3 = 0.05$ , and $\phi_{\text{plume}} = 20^\circ$
(A.4)	$a_4 = 1 \mu\text{g kg}^{-1}$ , $b_4 = 0.4$ , $c_4 = 2$ , and $\phi_q = 12^\circ$

$$\gamma = \frac{1}{\sigma_r + i\sigma_i} \left[ - \left( \frac{\partial \bar{\gamma}}{\partial y} + \frac{\partial \bar{T}}{\partial y} \frac{1}{\bar{S}} \frac{\partial \bar{\gamma}}{\partial p} \right) |v| \exp(i\varphi_v) - \frac{1}{\bar{S}} \frac{\partial \bar{\gamma}}{\partial p} (kc_i + i\sigma_r) |T| \exp(i\varphi_T) \right] \exp(i\theta) + \text{c.c.}, \quad (\text{B.5})$$

$$\overline{\text{GE}}(\mathbf{x}, p, t) = - \underbrace{C \left( \alpha_y + \frac{pf}{R} \frac{\partial \bar{u}}{\partial p} \alpha_p \right) [\sigma_i \cos(\varphi) + \sigma_r \sin(\varphi)] |v| |T|}_{\text{I}} - \underbrace{C(\sigma_i kc_i + \sigma_r^2) \alpha_p |T|^2}_{\text{II}}, \quad (\text{B.8})$$

where  $\overline{\text{GE}} = (c_p \bar{S})^{-1} \bar{q} \bar{T}$ ,  $\varphi = (\varphi_v - \varphi_T)$ , and

$$C = \frac{1}{2c_p \bar{S} (\sigma_r^2 + \sigma_i^2)} \exp(2kc_i t), \quad (\text{B.9})$$

$$\alpha_y(y, p; \bar{\gamma}) = A \frac{\partial \bar{\gamma}}{\partial y}, \quad \text{and} \quad (\text{B.10})$$

$$\alpha_p(y, p; \bar{\gamma}) = \frac{A}{\bar{S}} \frac{\partial \bar{\gamma}}{\partial p}. \quad (\text{B.11})$$

Equation (B.8) shows that the generation of eddy available potential energy  $\overline{\text{GE}}$  is due to dust-modified baroclinic effects (term I), which depend on the phasing  $\varphi$  between the wind and temperature fields, and dust-modified eddy available potential energy (term II). For our representative AEJ, the wind and temperature fields are  $180^\circ$  out of phase below the AEJ and in phase above the AEJ (see Figs. 5 and 6). Thus for term I in (B.8),  $\cos(\varphi) \approx \pm 1$  and  $\sin(\varphi) \approx 0$ . With these approximations, (B.8) simplifies to

$$\overline{\text{GE}} = G_1 |v| |T| + G_2 |T|^2, \quad (\text{B.12})$$

$$G_1 = \pm C \sigma_i \left( \alpha_y + \frac{pf}{R} \frac{\partial \bar{u}}{\partial p} \alpha_p \right), \quad \text{and} \quad (\text{B.13})$$

$$G_2 = -C(\sigma_i kc_i + \sigma_r^2) \alpha_p, \quad (\text{B.14})$$

where  $G_1$  in (B.13) is positive below the AEJ and negative above the AEJ.

where

$$\sigma_r = k(\bar{u} - c_r) \quad \text{and} \quad (\text{B.6})$$

$$\sigma_i = \left( kc_i - \frac{\alpha_p}{c_p} + D \right). \quad (\text{B.7})$$

The eddy dust mixing ratio [(B.5)] is controlled by the meridional and vertical gradients of the mean dust distribution, which arise from the advection of the mean dust by the eddy winds [see (B.2)]. From (B.5),  $\overline{\text{GE}}$  is obtained by 1) multiplying (B.5) by the dust transmissivity coefficient  $A$ , which yields the eddy dust heating rate and 2) multiplying the eddy dust-heating rate by the temperature  $T$  and then zonally averaging. The result is, after using the thermal wind relationship,

## REFERENCES

- Berry, G. J., and C. D. Thorncroft, 2012: African easterly wave dynamics in a mesoscale numerical model: The upscale role of convection. *J. Atmos. Sci.*, **69**, 1267–1283, doi:10.1175/JAS-D-11-099.1.
- Bretl, S., P. Reutter, C. C. Raible, S. Ferrachat, C. S. Poberaj, L. E. Revell, and U. Lohmann, 2015: The influence of absorbed solar radiation by Saharan dust on hurricane genesis. *J. Geophys. Res. Atmos.*, **120**, 1902–1917, doi:10.1002/2014JD022441.
- Burpee, R. W., 1972: The origin and structure of easterly waves in the lower troposphere of North Africa. *J. Atmos. Sci.*, **29**, 77–90, doi:10.1175/1520-0469(1972)029<0077:TOASOE>2.0.CO;2.
- , 1975: Some features of synoptic-scale wave based on a compositing analysis of GATE data. *Mon. Wea. Rev.*, **103**, 921–925, doi:10.1175/1520-0493(1975)103<0921:SFOSWB>2.0.CO;2.
- Carlson, T. N., 1969: Some remarks on African disturbances and their progress over the tropical Atlantic. *Mon. Wea. Rev.*, **97**, 716–726, doi:10.1175/1520-0493(1969)097<0716:SROADA>2.3.CO;2.
- , and C. B. Benjamin, 1980: Radiative heating rates for Saharan dust. *J. Atmos. Sci.*, **37**, 193–213, doi:10.1175/1520-0469(1980)037<0193:RHRFSD>2.0.CO;2.
- Chen, S.-H., and Y.-C. Liu, 2014: The relation between dry vortex merger and tropical cyclone genesis over the Atlantic Ocean. *J. Geophys. Res. Atmos.*, **119**, 11 641–11 661, doi:10.1002/2014JD021749.
- , S.-H. Wang, and M. Waylonis, 2010: Modification of Saharan air layer and environmental shear over the eastern Atlantic Ocean by dust-radiation effects. *J. Geophys. Res.*, **115**, D21202, doi:10.1029/2010JD014158.
- , Y.-C. Liu, T. R. Nathan, C. Davis, R. Torn, N. Sowa, C.-T. Cheng, and J.-P. Chen, 2015: Modeling the effects of

- dust-radiative forcing on the movement of Hurricane *Helene* (2006). *Quart. J. Roy. Meteor. Soc.*, **141**, 2563–2570, doi:10.1002/qj.2542.
- Cho, H.-R., and M. A. Jenkins, 1987: The thermal structure of tropical easterly waves. *J. Atmos. Sci.*, **44**, 2531–2539, doi:10.1175/1520-0469(1987)044<2531:TTSOTE>2.0.CO;2.
- Cordero, E. C., T. R. Nathan, and R. S. Echols, 1998: An analytical study of ozone feedbacks on Kelvin and Rossby-gravity waves: Effects on the QBO. *J. Atmos. Sci.*, **55**, 1051–1062, doi:10.1175/1520-0469(1998)055<1051:AASOOF>2.0.CO;2.
- Edmon, H. J., Jr., B. J. Hoskins, and M. E. McIntyre, 1980: Eliassen-Palm cross sections for the troposphere. *J. Atmos. Sci.*, **37**, 2600–2616, doi:10.1175/1520-0469(1980)037<2600:EPCSFT>2.0.CO;2.
- Engelstaedter, S., and R. Washington, 2007: Atmospheric controls on the annual cycle of North African dust. *J. Geophys. Res.*, **112**, D03103, doi:10.1029/2006JD007195.
- Frank, N. L., 1970: Atlantic tropical systems of 1969. *Mon. Wea. Rev.*, **98**, 307–314, doi:10.1175/1520-0493(1970)098<0307:ATSO>2.3.CO;2.
- Ghan, S. J., 1989a: Unstable radiative-dynamical interactions. Part I: Basic theory. *J. Atmos. Sci.*, **46**, 2528–2543, doi:10.1175/1520-0469(1989)046<2528:URIPB>2.0.CO;2.
- , 1989b: Unstable radiative-dynamical interactions. Part II: Expanded theory. *J. Atmos. Sci.*, **46**, 2544–2561, doi:10.1175/1520-0469(1989)046<2544:URDIP>2.0.CO;2.
- Grogan, D. F., T. R. Nathan, R. E. Echols, and E. C. Cordero, 2012: A parameterization for the effects of ozone on the wave driving exerted by equatorial waves in the stratosphere. *J. Atmos. Sci.*, **69**, 3715–3731, doi:10.1175/JAS-D-11-0343.1.
- Hall, N. M. J., G. N. Kiladis, and C. D. Thorncroft, 2006: Three-dimensional structure and dynamics of African easterly waves. Part II: Dynamical modes. *J. Atmos. Sci.*, **63**, 2231–2245, doi:10.1175/JAS3742.1.
- Hankes, I., Z. Wang, G. Zhang, and C. Fritz, 2015: Merger of African easterly waves and formation of Cape Verde storms. *Quart. J. Roy. Meteor. Soc.*, **141**, 1306–1319, doi:10.1002/qj.2439.
- Hess, M., P. Koepke, and I. Shult, 1998: Optical properties of aerosols and clouds: The software package OPAC. *Bull. Amer. Meteor. Soc.*, **79**, 831–844, doi:10.1175/1520-0477(1998)079<0831:OPOAAC>2.0.CO;2.
- Hosseinpour, F., and E. M. Wilcox, 2014: Aerosol interactions with African/Atlantic climate dynamics. *Environ. Res. Lett.*, **9**, 075004, doi:10.1088/1748-9326/9/7/075004.
- Hsieh, J.-S., and K. H. Cook, 2005: Generation of African easterly wave disturbances: Relationship to the African easterly jet. *Mon. Wea. Rev.*, **133**, 1311–1327, doi:10.1175/MWR2916.1.
- Ismail, S., and Coauthors, 2010: LASE measurements of water vapor, aerosol, and cloud distributions in Saharan air layers and tropical disturbances. *J. Atmos. Sci.*, **67**, 1026–1047, doi:10.1175/2009JAS3136.1.
- Jenkins, G. S., and A. Pratt, 2008: Saharan dust, lightning and tropical cyclones in the eastern tropical Atlantic during NAMMA-06. *Geophys. Res. Lett.*, **35**, L12804, doi:10.1029/2008GL033979.
- , —, and A. Heymsfield, 2008: Possible linkages between Saharan dust and tropical cyclone rain band invigoration in the eastern Atlantic during NAMMA-06. *Geophys. Res. Lett.*, **35**, L08815, doi:10.1029/2008GL034072.
- Jones, C., N. Mahowald, and C. Luo, 2003: The role of easterly waves on African desert dust transport. *J. Climate*, **16**, 3617–3628, doi:10.1175/1520-0442(2003)016<3617:TROEWO>2.0.CO;2.
- , —, and —, 2004: Observational evidence of African desert dust intensification of easterly waves. *Geophys. Res. Lett.*, **31**, L17208, doi:10.1029/2004GL020107.
- Jury, M. R., and M. J. Santiago, 2010: Composite analysis of dust impacts on African easterly waves in the Moderate Resolution Imaging Spectrometer era. *Geophys. Res. Lett.*, **115**, D16213, doi:10.1029/2009JD013612.
- Karyampudi, V. M., and T. N. Carlson, 1988: Analysis and numerical simulations of the Saharan air layer and its effect on easterly wave disturbances. *J. Atmos. Sci.*, **45**, 3102–3136, doi:10.1175/1520-0469(1988)045<3102:AANSOT>2.0.CO;2.
- , and H. F. Pierce, 2002: Synoptic-scale influence of the Saharan air layer on tropical cyclogenesis over the eastern Atlantic. *Mon. Wea. Rev.*, **130**, 3100–3128, doi:10.1175/1520-0493(2002)130<3100:SSIOTS>2.0.CO;2.
- , and Coauthors, 1999: Validation of the Saharan dust plume conceptual model using lidar, Meteosat, and ECMWF data. *Bull. Amer. Meteor. Soc.*, **80**, 1045–1075, doi:10.1175/1520-0477(1999)080<1045:VOTSDP>2.0.CO;2.
- Kaufman, Y. J., I. Koren, L. A. Remer, D. Tanré, P. Ginoux, and S. Fan, 2005: Dust transport and deposition observed from Terra-Moderate Resolution Imaging Spectroradiometer (MODIS) spacecraft over the Atlantic Ocean. *J. Geophys. Res.*, **110**, D10S12, doi:10.1029/2003JD004436.
- Knippertz, P., and M. C. Todd, 2010: The central west Saharan dust hot spot and its relation to African easterly waves and extratropical disturbances. *Geophys. Res. Lett.*, **115**, D12117, doi:10.1029/2009JD012819.
- Kocha, C., J.-P. Lafore, P. Tulet, and Y. Seity, 2012: High-resolution simulation of major West African dust-storm: Comparison with observations and investigation of dust impact. *Quart. J. Roy. Meteor. Soc.*, **138**, 455–470, doi:10.1002/qj.927.
- Konare, A., A. S. Zakey, F. Solmon, F. Giorgi, S. Rauscher, S. Ibrah, and X. Bi, 2008: A regional climate modeling study of the effect of desert dust on the West African monsoon. *J. Geophys. Res.*, **113**, D12206, doi:10.1029/2007JD009322.
- Kwon, H. J., 1989: A reexamination of genesis of African waves. *J. Atmos. Sci.*, **46**, 3621–3631, doi:10.1175/1520-0469(1989)046<3621:AROTGO>2.0.CO;2.
- Landsea, C. W., 1993: A climatology of intense (or major) Atlantic hurricanes. *Mon. Wea. Rev.*, **121**, 1703–1713, doi:10.1175/1520-0493(1993)121<1703:ACOIMA>2.0.CO;2.
- Lavaysse, C., J.-P. Chadboureau, and C. Flamant, 2011: Dust impact on the West African heat low in summertime. *Quart. J. Roy. Meteor. Soc.*, **137**, 1227–1240, doi:10.1002/qj.844.
- Leroux, S., and N. M. J. Hall, 2009: On the relationship between African easterly waves and the African easterly jet. *J. Atmos. Sci.*, **66**, 2303–2316, doi:10.1175/2009JAS2988.1.
- Ma, P.-L., K. Zhang, J. J. Shi, T. Matsui, and A. Arking, 2012: Direct radiative effect of mineral dust on the development of African easterly waves. *J. Appl. Meteor. Climatol.*, **51**, 2090–2104, doi:10.1175/JAMC-D-11-0215.1.
- Mekonnen, A., C. D. Thorncroft, and A. R. Aiyer, 2006: Analysis of convection and its association with African easterly waves. *J. Climate*, **19**, 5405–5421, doi:10.1175/JCLI3920.1.
- Moulin, C., and I. Chiappello, 2004: Evidence of the control of summer atmospheric transport of African dust over the Atlantic by Sahel source from TOMS satellites (1979–2000). *J. Geophys. Res.*, **31**, L02107, doi:10.1029/2003GL018931.
- Nathan, T. R., 1989: On the role of ozone in the stability of Rossby normal modes. *J. Atmos. Sci.*, **46**, 2094–2100, doi:10.1175/1520-0469(1989)046<2094:OTROOI>2.0.CO;2.

- , and L. Li, 1991: Linear stability of free planetary waves in the presence of radiative–photochemical feedbacks. *J. Atmos. Sci.*, **48**, 1837–1855, doi:10.1175/1520-0469(1991)048<1837:LSOFPW>2.0.CO;2.
- , and E. C. Cordero, 2007: An ozone-modified refractive index for vertically propagating planetary waves. *J. Geophys. Res.*, **112**, D02105, doi:10.1029/2006JD007357.
- Norquist, D. C., E. E. Recker, and R. J. Reed, 1977: The energetics of African wave disturbances as observed during phase III of GATE. *Mon. Wea. Rev.*, **105**, 334–342, doi:10.1175/1520-0493(1977)105<0334:TEOAWD>2.0.CO;2.
- Paradis, D., J.-P. Lafore, J.-L. Redelsperger, and V. Balaji, 1995: African easterly waves and convection. Part I: Linear simulations. *J. Atmos. Sci.*, **52**, 1657–1679, doi:10.1175/1520-0469(1995)052<1657:AEWACP>2.0.CO;2.
- Prospero, J. M., 1999: Long-range transport of mineral dust in the global atmosphere: Impact of African dust on the environment of the southeastern United States. *Proc. Natl. Acad. Sci. USA*, **96**, 3396–3403, doi:10.1073/pnas.96.7.3396.
- , and T. N. Carlson, 1972: Vertical and areal distributions of Saharan dust over the western equatorial North Atlantic Ocean. *J. Geophys. Res.*, **77**, 5255–5265, doi:10.1029/JC077i027p05255.
- Pytharoulis, I., and C. Thorncroft, 1999: The low-level structure of African easterly waves in 1995. *Mon. Wea. Rev.*, **127**, 2266–2280, doi:10.1175/1520-0493(1999)127<2266:TLLSOA>2.0.CO;2.
- Reale, O., W. K. Lau, K.-M. Kim, and E. Brin, 2009: Atlantic tropical cyclogenetic processes during SOP-3 NAMMA in the GEOS-5 global data assimilation and forecast system. *J. Atmos. Sci.*, **66**, 3563–3578, doi:10.1175/2009JAS3123.1.
- , K. M. Lau, and A. D. Silva, 2011: Impact of an interactive aerosol on the African easterly jet in the NASA GOES-5 global forecasting system. *Wea. Forecasting*, **26**, 504–519, doi:10.1175/WAF-D-10-05025.1.
- Rennick, M. A., 1976: The generation of African waves. *J. Atmos. Sci.*, **33**, 1955–1969, doi:10.1175/1520-0469(1976)033<1955:TGOAW>2.0.CO;2.
- Ross, R. S., and T. N. Krishnamurti, 2007: Low-level African easterly wave activity and its relation to Atlantic tropical cyclogenesis in 2001. *Mon. Wea. Rev.*, **135**, 3950–3964, doi:10.1175/2007MWR1996.1.
- Thorncroft, C. D., and B. J. Hoskins, 1994: An idealized study of African easterly waves. I: Linear theory. *Quart. J. Roy. Meteor. Soc.*, **120**, 953–982, doi:10.1002/qj.49712051809.
- , N. M. J. Hall, and G. N. Kiladis, 2008: Three-dimensional structure and dynamics of African easterly waves. Part III: Genesis. *J. Atmos. Sci.*, **65**, 3596–3607, doi:10.1175/2008JAS2575.1.
- Tompkins, A. M., C. Cardinali, J.-J. Morcrette, and M. Rodwell, 2005: Influence of aerosol climatology on forecasts of the African easterly jet. *Geophys. Res. Lett.*, **32**, L10801, doi:10.1029/2004GL022189.
- Wang, Y., 1995: An inverse balance equation in sigma coordinates for model initialization. *Mon. Wea. Rev.*, **123**, 482–488, doi:10.1175/1520-0493(1995)123<0482:AIBEIS>2.0.CO;2.
- Wilcox, E. M., K. M. Lau, and K.-M. Kim, 2010: A northward shift of the North Atlantic Ocean intertropical convergences zone in response to summertime Saharan dust outbreaks. *Geophys. Res. Lett.*, **37**, L04804, doi:10.1029/2009GL041774.
- Zhu, A., V. Ramanathan, F. Li, and D. Kim, 2007: Dust plumes over the Pacific, Indian, and Atlantic oceans: Climatology and radiative impact. *J. Geophys. Res.*, **112**, D16208, doi:10.1029/2007JD008427.
- Zhu, X., and J. R. Holton, 1986: Photochemical damping of inertio–gravity waves. *J. Atmos. Sci.*, **43**, 2578–2584, doi:10.1175/1520-0469(1986)043<2578:PDOIW>2.0.CO;2.